HHS Public Access

Author manuscript

Mol Cell. Author manuscript; available in PMC 2023 August 18.

Published in final edited form as:

Mol Cell. 2022 August 18; 82(16): 3030–3044.e8. doi:10.1016/j.molcel.2022.06.003.

An Oncogenic JMJD6-DGAT1 Axis Tunes Epigenetic Regulation of Lipid Droplet Formation in Clear Cell Renal Cell Carcinoma

Jin Zhou[1], **Jeremy M. Simon**[2,3,4], **Chengheng Liao**[1], **Cheng Zhang**[1], **Lianxin Hu**[1], **Giada Zurlo**[1], **Xijuan Liu**[2], **Cheng Fan**[2], **Austin Hepperla**[2,3,4], **Liwei Jia**[1], **Vanina Toffessi Tcheuyap**[5,6], **Hua Zhong**[1,7], **Roy Elias**[5,6], **Jin Ye**[8], **W. Mike Henne**[9], **Payal Kapur**[1,5], **Deepak Nijhawan**[6,10], **James Brugarolas**[5,6], **Qing Zhang**[1,5,11,*]

[1]Department of Pathology, University of Texas Southwestern Medical Center, Dallas, TX 75390, USA

[2]Lineberger Comprehensive Cancer Center, University of North Carolina School of Medicine, Chapel Hill, NC 27599, USA

[3]Department of Genetics, Neuroscience Center, University of North Carolina, Chapel Hill, NC 27599, USA

[4]UNC Neuroscience Center, Carolina Institute for Developmental Disabilities, University of North Carolina, Chapel Hill, NC 27599, USA

[5]Kidney Cancer Program, Simmons Comprehensive Cancer Center, University of Texas Southwestern Medical Center, Dallas, TX 75390, USA

[6]Department of Internal Medicine, University of Texas Southwestern Medical Center, Dallas, TX 75390, USA

[7]Lyda Hill Department of Bioinformatics, University of Texas Southwestern Medical Center, Dallas, TX 75390, USA

[*]**Corresponding author:** Qing.Zhang@UTSouthwestern.edu.

AUTHOR CONTRIBUTIONS

Conception and design: J.Z., Q.Z.; Acquisition of data: J.Z., V.T., W.M.H., Y.J., J.B., Q.Z.; Analysis and interpretation of data: J.Z., J.S., A.H., H.Z., L.J., P.K., R.E., Q.Z.; Writing, review, and/or revision of the manuscript: J.Z., J.S., G.Z., L.J., W.M.H., D.N., J.B., Q.Z.; Administrative, technical, or material support: J.Z., G.Z., C.Z., L.H., C.L., X.L., W.M.H., V.T., D.N., J.B., Q.Z.; Study supervision: J.B., Q.Z.

DECLARATION OF INTERESTS

The authors declare no competing interests.

SUPPORTING CITATIONS

The following references appear in the supplemental information: (Liu et al., 2020; Melo et al., 2011)

INCLUSION AND DIVERSITY

We worked to ensure gender balance in the recruitment of human subjects. We worked to ensure sex balance in the selection of non-human subjects. We worked to ensure diversity in experimental samples through the selection of the cell lines. One or more of the authors of this paper self-identifies as an underrepresented ethnic minority in science. One or more of the authors of this paper self-identifies as living with a disability. While citing references scientifically relevant for this work, we also actively worked to promote gender balance in our reference list. The author list of this paper includes contributors from the location where the research was conducted who participated in the data collection, design, analysis, and/or interpretation of the work.

[8]Department of Molecular Genetics, University of Texas Southwestern Medical Center, Dallas, TX 75390, USA

[9]Department of Cell Biology, University of Texas Southwestern Medical Center, Dallas, TX 75390, USA

[10]Department of Biochemistry, University of Texas Southwestern Medical Center, Dallas, TX 75390, USA

[11]Lead contact

SUMMARY

Characterized by intracellular lipid droplet accumulation, clear cell renal cell carcinoma (ccRCC) is resistant to cytotoxic chemotherapy and is a lethal disease. Through an unbiased siRNA screen of 2-oxoglutarate (2-OG)-dependent enzymes, which play a critical role in tumorigenesis, we identified *Jumonji domain-containing 6* (*JMJD6*) as an essential gene for ccRCC tumor development. Downregulation of JMJD6 abolished ccRCC colony formation *in vitro* and inhibited orthotopic tumor growth *in vivo*. Integrated ChIP-seq and RNA-seq analyses uncovered diacylglycerol O-acyltransferase 1 (DGAT1) as a critical JMJD6 effector. Mechanistically, JMJD6 interacted with RBM39, co-occupied *DGAT1* gene promoter with H3K4me3 to induce *DGAT1* expression. *JMJD6* silencing reduced DGAT1, leading to decreased lipid droplet formation and tumorigenesis. Pharmacological inhibition (or depletion) of DGAT1 inhibited lipid droplet formation *in vitro* and ccRCC tumorigenesis *in vivo*. Thus, the JMJD6-DGAT1 axis represents a potential new therapeutic target for ccRCC.

Graphical Abstract

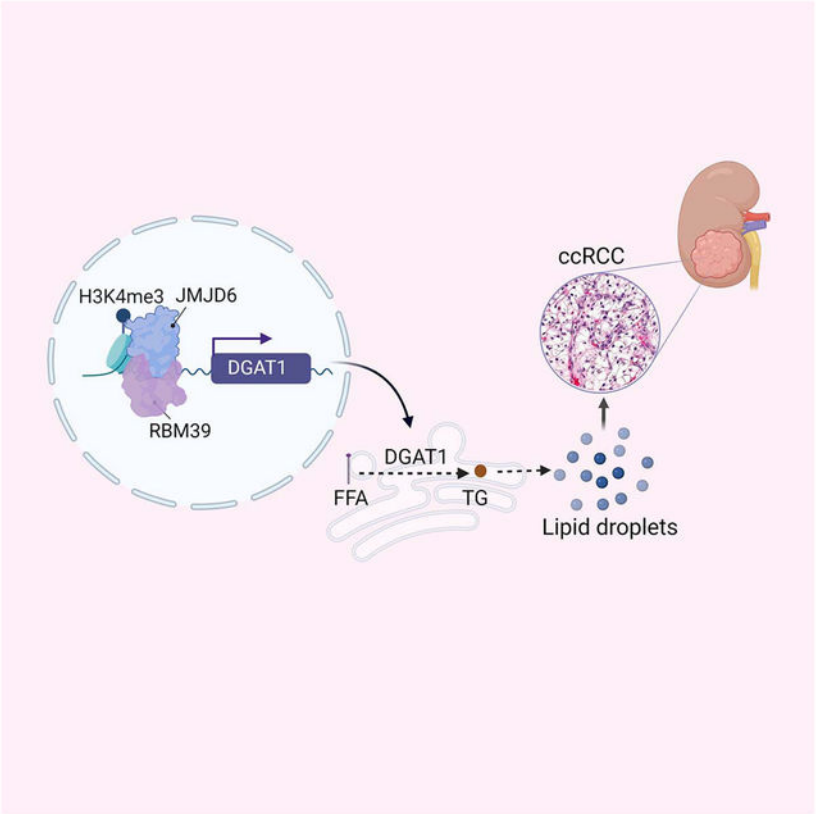

eTOC blurb

Zhou et al. reveal that JMJD6 promotes *DGAT1* expression in an enzymatic-independent manner, which is essential for lipid droplet formation and tumorigenesis in ccRCC. DGAT1 depletion or inhibition leads to decreased ccRCC tumorigenesis, suggesting a potential therapeutic option in this lethal cancer.

Keywords

ccRCC; 2-OG-dependent dioxygenases; JMJD6; DGAT1; lipid droplet

INTRODUCTION

The incidence of kidney cancer has been increasing steadily for the past several decades, although the reasons for this are unclear (Godwin et al., 2014). The estimated number of new cases and deaths from renal cancer in 2020 in the U.S. are 73,750 and 14,830, respectively (Siegel et al., 2020). Clear cell renal cell carcinoma (ccRCC) accounts for approximately 85% of all kidney cancers and is characterized by mutation in the *von Hippel-Lindau (VHL)* tumor suppressor gene (Kaelin, 2002). VHL inactivation leads to hypoxia-inducible factor (HIF) signaling, but it remains challenging to target HIF (Chen et al., 2016; Cho et al., 2016).

ccRCCs are characterized by intracellular lipid accumulation. ccRCCs are enriched for lipid droplets that consist of a neutral lipid core containing triglycerides (TG) and cholesterol-esters surrounded by a phospholipid monolayer and associated surface proteins (Qiu et al., 2015; Walther and Farese, 2012). Two well-characterized functions of lipid storage in eukaryotic cells include energy homeostasis and lipid release for membrane synthesis during proliferation. How lipids accumulate in ccRCC is not completely understood. Some evidence suggests that HIF2 promotes lipid storage by regulating perilipin 2 (PLIN2) (Qiu et al., 2015). However, lipid droplet formation may also occur independently of HIF2 (Lee et al., 2017; Sethi et al., 2017).

2-oxoglutarate (2-OG) dependent enzymes belong to a family of enzymes that use oxygen, Fe^{2+}, and 2-OG for catalysis. This family includes prolyl hydroxylases, histone demethylases and DNA hydroxylases (Losman and Kaelin, 2013), which are involved in the pathogenesis of cancer including ccRCC. For example, prolyl hydroxylases modulate the abundance of HIF_{α}, FOXO3a and adenylosuccinate lyase (ADSL) and regulate cancer cell growth (Zheng et al., 2014; Zurlo et al., 2019). By regulating H3K4 and H3K36 methylation, histone demethylases control gene expression and have been linked to the pathogenesis of several cancers (Cloos et al., 2008; Varier and Timmers, 2011). The function of Tet DNA hydroxylases has been well documented in hematological malignancies (Losman and Kaelin, 2013). However, a systematic and unbiased approach to screen for critical enzymes that may play important roles in ccRCC is lacking.

Through an unbiased siRNA screen in ccRCC cells, we identified *JMJD6* as an important gene for ccRCC cell growth and tumorigenesis. JMJD6 is an enzyme with *N*-methyl arginyl demethylase and lysyl C-5 hydroxylase activities (Bottger et al., 2015). However, besides acting as an enzyme, JMJD6 was also reported to control gene expression through enhancer-mediated transcriptional pause-release mechanisms (Liu et al., 2013; Miller et al., 2017). In this study, we identified a novel role of JMJD6, which co-occupies target gene promoter regions characterized by tri-methylation of lysine 4 on histone H3 (H3K4me3) and H3K27 acetylation (H3K27ac), leading to the activation of genes critical for ccRCC development. Furthermore, we identified DGAT1 as a critical effort downstream implicated in lipid droplet formation and tumor development.

RESULTS

siRNA Screen Implicates JMJD6 in ccRCC Tumor Cell Proliferation

In order to identify novel 2-OG dependent enzymes that may contribute to ccRCC cell growth, we performed an siRNA screen using an ON-TARGETplus siRNA library of all enzymes in the 2-OG family. We developed a screening method based on 3D anchorage-independent growth (Figure S1A and S1B). We used non-targeting sequences as a negative control and a house-keeping gene (Lamin A/C) as a positive control (FigureS1C). By using this approach and a representative ccRCC cell line (UMRC2), we identified ~20 enzymes that impaired 3D growth upon depletion (Figure 1A). In order to explore candidate oncogenes emerging from our screen and assess their relevance in ccRCC, we examined their expression in ccRCC. We focused on genes that fit the following 3 criteria: (1) their depletion led to decreased soft-agar colony growth; (2) their expression was higher in

ccRCC tumors compared to normal kidney tissue in a TCGA ccRCC dataset; and (3) their overexpression was associated with worse ccRCC prognosis. With these criteria, we were able to narrow down the list to the following 7 genes: *TET3*, *KDM4B*, *JMJD4*, *JMJD6, P4HB, PLOD2*, and *PLOD3* (Figure S1D and S1E). Among them, TET3 (Chen et al., 2017), P4HB (Xie et al., 2020b; Zhu et al., 2019), PLOD2 (Xu et al., 2020), and PLOD3 (Xie et al., 2020a) have been reported to be prognostic markers or oncogenes in ccRCC.

Next, we examined the effect of individual siRNA in the screening pool. JMJD6 targeting with four independent siRNAs profoundly inhibited ccRCC cell growth (Figure S1F). In keeping with our set criteria, *JMJD6* was highly expressed in ccRCC tumors and high *JMJD6* levels were associated with worse prognosis (Figure S1G and S1H). We were also interested in JMJD6, as it may also modulate tumor responsiveness to therapy (Zhang et al., 2021).

To further validate the findings from our siRNA screen, we transfected 3 ccRCC cell lines (UMRC2, 786-O, and A-498) with two individual *JMJD6* siRNAs and examined the impact on cell proliferation, 2D colony formation and 3D soft agar growth. *JMJD6* depletion with independent siRNAs decreased cell proliferation (Figure S1I and S1J), colony formation, and soft agar growth in all ccRCC cell lines (Figure S1K-M).

Next, we examined the effect of persistent *JMJD6* knockdown using two independent shRNAs (#3, #4) in multiple ccRCC cell lines (786-O, UMRC2, and UMRC6). *JMJD6* knockdown by shRNA also led to decreased cell proliferation, colony formation, and 3D soft agar growth (Figure 1B-E; Figure S1N).

The role of JMJD6 in ccRCC is independent of its catalytic activity

To further evaluate the role of *JMJD6* in ccRCC, we used CRISPR-Cas9 gene editing. Consistent with our previous results, *JMJD6* knockout inhibited ccRCC colony formation and 3D soft agar growth (Figure 1F-J). In contrast, *JMJD6* depletion in a representative normal renal epithelial cell line (HKC) did not affect cell proliferation and only slightly reduced colony formation (Figure 1F-J). To determine whether the phenotype associated with sgRNA targeting was on-target, we restored *JMJD6* expression using a sgRNA resistant version (Figure 1K). We found that wild type (WT) *JMJD6* rescued the growth of *JMJD6*-depleted cells as well as colony formation (Figure 1L-N).

To determine whether JMJD6 catalytic activity was required, we introduced instead a JMJD6 catalytic dead (CD) mutant (H187A/D189A) (Wang et al., 2014). Interesting, the CD mutant also largely rescued the phenotype of *JMJD6* knockout cells (Figure 1K-N). To corroborate this finding, we leveraged a JMJD6 inhibitor, WL12 (Ran et al., 2019). WL12 had minimal effects on multiple ccRCC cell lines (Figure S1O-Q). In summary, our results show that JMJD6 is essential for ccRCC cell proliferation and tumorigenesis independently of its enzymatic activity.

JMJD6 is Involved in ccRCC Tumor Growth

To examine the ability of JMJD6 to maintain ccRCC tumor growth, we generated UMRC2 and 786-O cells with a doxycycline-inducible *JMJD6* shRNA. Doxycycline

addition depleted JMJD6 (Figure 2A and 2B) and decreased cell proliferation, 2D colony formation, and 3D soft agar colony formation (Figure 2C-H). Next, we injected ccRCC cells with the doxycycline inducible *JMJD6* shRNA (or control shRNA) that were labeled with firefly luciferase orthotopically (under the kidney capsule) in NoD SCID γc (NSG) mice. Successful implantation and growth of ccRCC cells was established through weekly bioluminescence imaging. Once tumors had reached a certain size, we fed these mice doxycycline. Over the course of a 6-week treatment, we observed decreased tumor growth (Figure 2I and 2J). Doxycycline effectively depleted *JMJD6* by immunoblotting and IHC staining (Figure 2K; Figure S2A) and decreased tumor weight and tumor size (Figure 2L and 2M). Notably, *JMJD6* depletion also reduced lung metastases (Figure 2N and 2O).

Next, we examined JMJD6 dysregulation in ccRCC in patients at our UTSW Kidney Cancer Specialized Program of Research Excellence (SPORE) program. We first examined *JMJD6* mRNA levels in normal and paired ccRCC tumors (n=41) (European Genome-Phenome Archive, EGAS00001005516). *JMJD6* was highly expressed in tumors compared to normal controls (Figure 2P). To extend these results to protein analyses, we performed IHC staining for 20 pairs of ccRCCs. As determined using *H scores* (which combined as both the frequency and intensity of expression (Fedchenko and Reifenrath, 2014)), JMJD6 was prominently expressed in ccRCC (Figure 2Q and 2R; Figure S2B). We complemented these studies by examining *JMJD6* expression in our patient derived tumorgraft (PDX) platform (Elias et al., 2021; Sivanand et al., 2012). We found that *JMJD6* was highly expressed in PDXs as well (Figure S2C).

JMJD6 Regulation in ccRCC is VHL and HIF Independent

Next, we evaluated whether JMJD6 upregulation was associated with *VHL* loss using ccRCC tumor samples with categorized *VHL* mutation information as described previously (Zhang et al., 2018). We found that higher JMJD6 in ccRCC tumors regardless of *VHL* mutation (Figure S2D), suggesting that JMJD6 upregulation is independent of *VHL*. To further examine this, we restored *VHL* in ccRCC cell lines with defective *VHL* and found that JMJD6 protein levels were unaffected (Figure S2E). To determine whether canonical HIF signaling was important for JMJD6 regulation, we depleted Aryl Hydrocarbon Receptor Nuclear Translocator (ARNT), which is an obligatory partner for HIFα subunits and is necessary for HIF activity. JMJD6 protein level was unaffected by *ARNT* knockout (Figure S2F). In summary, JMJD6 is important for maintaining ccRCC tumor growth *in vivo* and its upregulation in ccRCC tumors is independent of VHL and HIF.

JMJD6 Promotes Gene Expression by Occupying Target Gene Promoters

JMJD6 has been previously shown to bind chromatin and our data suggest that its role in ccRCC is independent of its enzymatic activity. In order to investigate the molecular mechanism by which JMJD6 regulates ccRCC cell proliferation, we performed JMJD6 ChIP-seq using wild-type 786-O cells and RNA-seq analyses using wild-type 786-O cells transduced with a control sgRNA as well as *JMJD6* knockout cells transduced with two independent *JMJD6* sgRNAs. We complemented the JMJD6 ChIP-seq studies with H3K4me3 ChIP-seq and integrated these data with ChIP-seq data from HIF1β, HIF2α, H3K4me1, and H3K27ac from previous publications (Yao et al., 2017). We found that

JMJD6 binding sites frequently overlapped with H3K4me3 (73.8% overlap), but not overlapping significantly with H3K4me1 (44%), HIF1β (< 1%), or HIF2α (< 1%) (Figure 3A). Thus, we focused our attention on genes whose expression may be positively regulated by JMJD6. By overlapping JMJD6 positively-regulated genes (by RNA-seq) with JMJD6-bound promoters, we identified 64 genes within 5 kb of the transcription start site (TSS) (Table S4). To further narrow down the list, we sought genes that: (1) contained JMJD6 binding sites in the promoter and were characterized by H3K4me3 and H3K27ac; (2) were positively regulated by JMJD6 (as determined by their downregulation following *JMJD6* silencing); and (3) were associated with worse prognosis in ccRCC patients (Cancer Genome Atlas Research, 2013). By combining these parameters, we narrowed down the JMJD6 direct target gene list to 5 genes: *Major facilitator superfamily domain containing 3* (*MFSD3*), *diacylglycerol O-acyltransferase 1* (*DGAT1*), *Zinc Finger SWIM-Type Containing 8* (*ZSWIM8*), *DnaJ Heat Shock Protein Family Member B12* (*DNAJB12*), and *Importin 13* (*IPO13*) (Figure 3A). We visually examined the ChIP-seq data for these genes and found that, as expected, their promoters were enriched for JMJD6, H3K4me3, and H3K27ac (Figure 3B). Next, we examined the binding patterns of JMJD6, H3K4me3, H3K27ac on these target gene promoters and further tested JMJD6 enrichment using ChIP-qPCR. We found that JMJD6 localized to these five target genes, but not at a local negative control site, exhibiting significant enrichment when compared to IgG (Figure 3C). RT-PCR analyses showed consistent downregulation in 3 genes (*DGAT1*, *MFSD3*, and *ZSWIM8*) by two independent *JMJD6* sgRNAs (Figure 3D). Importantly, *DGAT1, MFSD3*, and *ZSWIM8* downregulation by *JMJD6* knockout could be completely rescued by a sgRNA-resistant *JMJD6* construct. Consistent with the notion that JMJD6 catalytic activity is dispensable for this regulation, JMJD6-CD also rescued the expression of these genes (Figure 3E). In addition, JMJD6-CD was similarly enriched at target gene promoters by ChIP-qPCR (Figure S3A). However, promoter enrichment on some target genes (such as DGAT1, ZSWIM8, IPO13) was higher for WT JMJD6 compared to CD. In other cases, WT and CD JMJD6 behaved similarly (such as MFSD3 and DNAJB12).

Since our data showed that JMJD6 overlapped primarily with H3K4me3 (Figure 3A), which we also observed with decreased H3K4me3 occupancy on *DGAT1/ZSWIM8/ IPO13* gene promoters following JMJD6 knockout (Figure 3F). We also investigated the potential for cooperative binding of JMJD6 with H3K4 methyltransferases including SET Domain Containing 1A (SETD1A), mixed-lineage leukemia 1 (MLL1), and MLL2 as well as RNA polymerase II (pol II) (Liu et al., 2013). Consistent with a previous study showing that JMJD6 bound DNA cooperatively with pol II (Liu et al., 2013), JMJD6 co-immunoprecipitated with pol II, but not with any of the methyltransferases tested (Figure S3B). Interestingly, pol II enrichment at *DGAT1* and *IPO13* promoters decreased following JMJD6 knockout (Figure S3C). A modest decrease in pol II occupancy was observed with a second *JMJD6* sgRNA but it did not reach statistical significance. To summarize, our data suggests that JMJD6 directly regulate the gene expression of these downstream targets, which may play an important role in ccRCC.

DGAT1 Expression is Controlled by JMJD6 and is Essential for ccRCC Cell Proliferation

We next explored the expression of JMJD6 target genes between ccRCC tumors and matched normal kidneys, and found that *DNAJB12, ZSWIM8*, and *DGAT1* were overexpressed in ccRCC whereas *IPO13* and *MFSD3* were under expressed (Figure S4A). We also investigated whether their gene expression correlated with *JMJD6*. Whereas *DNAJB12, ZSWIM8*, and *DGAT1* were positively correlated with *JMJD6* at the mRNA level, *IPO13* and *MFSD3* were negatively correlated (Figure S4B). We examined the protein levels of these JMJD6 target genes by western blot following JMJD6 knockout(there is no commercial antibody available to reliably detect ZSWIM8) (Han et al., 2020). Our results showed that DGAT1 and IPO13 were reduced in 786-O cells upon JMJD6 knockout, whereas no change was observed for the other JMJD6 targets (Figure 4A).

In order to further narrow down JMJD6 target genes important for ccRCC tumorigenesis, we performed rescue experiments. We found that only DGAT1 overexpression partially rescued the phenotype of JMJD6 knockout in ccRCC (Figure 4B-D; Figure S4C-O). Thus, DGAT1 serves as a major target downstream of JMJD6 in ccRCC tumorigenesis. We further analyzed *DGAT1* mRNA expression in PDXs (Sivanand et al., 2012) and found that *DGAT1* was overexpressed in PDXs compared with matched normal tissues (Figure 4E). In addition, higher *DGAT1* expression predicted worse prognosis in ccRCC (Figure 4F). Next, we examined DGAT1 levels in 20 pairs of ccRCC tumor and normal tissue, and we found that JMJD6 and DGAT1 protein levels were more abundant in tumors, and they displayed a moderate correlation (Figure 4G and 4H; Figure S4P-R). All these results motivated us to study the role of *DGAT1* in mediating the effect of JMJD6 in ccRCC.

To determine whether the effect of *JMJD6* sgRNAs on *DGAT1* expression was on-target, we performed rescue experiments. We found that the effect of *JMJD6* silencing on *DGAT1* expression could be rescued by restoration of *JMJD6* with an sgRNA-resistant version (Figure 4I). In addition, exogenous overexpression of *JMJD6* (based on endogenous *JMJD6* levels) further increased *DGAT1* expression (Figure S4S and S4T), suggesting that *JMJD6* is both necessary and sufficient to regulate *DGAT1*. Consistent with our data that JMJD6 enzymatic activity may not be critical for ccRCC cell proliferation, both JMJD6-WT and JMJD6-CD rescued DGAT1 protein levels (Figure S4U). Additionally, JMJD6-WT could still rescue DGAT1 protein expression despite inhibition of its activity by the JMJD6 inhibitor WL12 (Figure S4V). To examine the importance of DGAT1 signaling in ccRCC, we first infected 786-O and UMRC2 cells with *DGAT1* shRNAs (sh1, sh2) and found that *DGAT1* knockdown decreased 2D colony formation and 3D soft agar growth (Figure 4J-M). In addition, we also used CRISPR-Cas9 guided sgRNAs (sg2, sg3) to achieve *DGAT1* depletion and consistently observed decreased colony formation in UMRC2 cells with *DGAT1* knockout (Figure 4N-Q).

To understand mechanistically on how JMJD6 contributes to ccRCC tumorigenesis by transactivating DGAT1, we used mass spectrometry to identify proteins that interact with JMJD6 in ccRCC cells. Among these proteins, we identified some known JMJD6 interaction proteins (Figure 4R), such as LUC7L2 (Webby et al., 2009), PPIL4 (Barak et al., 2021), PHRF1 (Fages et al., 2020). In addition, we used western blotting to validate that both Cleavage and Polyadenylation Specific Factor 6 (CPSF6) and RNA Binding Motif Protein

39 (RBM39) interacted with JMJD6 in ccRCC cells (Figure S4W). It is worth noting that a prior study also determined that JMJD6 co-purified with endogenous RBM39 in H1155 lung carcinoma cells (Han et al., 2017). By applying either siRNAs or shRNAs against CPSF6 or RBM39, we found that CPSF6 knockdown did not lead to downregulation of DGAT1 in 786-O cells (Figure S4X), while depletion of RBM39 led to decreased DGAT1 protein level (Figure 4S). RBM39 is an RNA-binding protein that acts as a pre-mRNA splicing factor but can also acts as a transcriptional coactivator (Dowhan et al., 2005; Loerch et al., 2014). To address the hypothesis that a RBM39-JMJD6 complex transcriptionally regulates DGAT1 expression, we measured the mRNA level of DGAT1 by RT-qPCR upon RBM39 depletion. DGAT1 mRNA levels decreased upon RBM39 depletion in all of ccRCC cell lines we tested (Figure 4T). Indisulam and related sulfonamides are pharmacologic tools to assess the role of RBM39 by selectively degradation through the ubiquitin-proteasome pathway (Han et al., 2017; Uehara et al., 2017). Consistent with our prior experiments using RBM39 RNAi, these results showed that indisulam treatment led to decreased DGAT1 expression at both the mRNA and protein level (Figure 4U and 4V), although different ccRCC cell lines displayed different sensitivity to Indisulam.

To examine whether RBM39 mediates the effect of JMJD6 on DGAT1 expression, we overexpressed JMJD6 followed by depletion of RBM39 by the shRNA used in the experiment above, then we examined DGAT1 expression and performed H3K4me3 ChIP-PCR for DGAT1 locus. The result showed that DGAT1 expression level was increased upon JMJD6 overexpression, the effect ameliorated with concurrent RBM39 depletion measured by both mRNA and protein level in 786-O cells (Figure 4W; Figure S4Y), and JMJD6 overexpression also led to increased H3K4me3 occupancy at DGAT1 locus, the effect abrogated by concurrent RBM39 depletion (Figure 4X). In addition, we found that both wildtype and catalytic dead (CD) JMJD6 can interact with RBM39 (Figure S4Z), indicating that RBM39-JMJD6 interaction is independent of enzymatic activity. To summary, RBM39 is involved in the transcriptional regulation of JMJD6 on DGAT1.

The JMJD6-DGAT1 Signaling Axis Controls Lipid Droplet Formation in ccRCC

DGAT1 is a TG synthase required for storage of intracellular lipids, and may play a role in ccRCC, which is characterized by lipid accumulation and gives rise to its characteristic clear cell histology (Qiu et al., 2015; Walther and Farese, 2012). Two well-characterized functions of lipid storage in eukaryotic cells include energy homeostasis and release of lipids for membrane synthesis during proliferation (Qiu et al., 2015). In order to examine whether the formation of lipid droplets is important for RCC growth, we used Triacsin C, an inhibitor of *de novo* synthesis of fatty acids and subsequent TG storage (Piccolis et al., 2019). We treated both normal renal cells and ccRCC cells (UMRC2). ccRCC cells displayed increased sensitivity towards Triacsin C treatment (1 μM dose) (Figure S5A). Interestingly, Triacsin C treatment in 786-O cells dampened the effect of JMJD6 overexpression (Figure S5B), suggesting that lipid droplet formation is at least partially responsible for the effect of JMJD6 on ccRCC cell growth.

As DGAT1 is an important triglyceride synthase for lipid droplets, we postulated that JMJD6-DGAT1 may contribute to lipid droplet formation in ccRCC. First, we examined

lipid droplet formation by using two different dyes (HCS LipidTOX™ and Bodipy) in ccRCC cells with *DGAT1* knockout and found that *DGAT1* depletion consistently decreased lipid droplet formation (Figure 5A-C). The DGAT1 inhibitor A922500, a highly specific inhibitor (King et al., 2009), also decreased lipid droplet formation (Figure 5D and 5E). A922500 did not, however, cause a significant change in lipid droplet formation in normal HKC (Figure S5C and S5D). In addition, A922500 decreased TG formation in ccRCC cells (UMRC2 and 786-O) but not in normal HKC cells (Figure S5E). Since JMJD6 regulates DGAT1 levels, we also examined the effect of JMJD6 on lipid droplet formation and found that *JMJD6* depletion by multiple sgRNAs reduced lipid droplet formation in ccRCC (Figure 5F and 5G). More importantly, *DGAT1* overexpression in *JMJD6* knockdown cells partially rescued the effect of *JMJD6* knockout (Figure 5H and 5I). Rescue experiments with JMJD6 CD mutant confirmed that the effect of JMJD6 on lipid droplet formation was largely independent of enzymatic activity (Figure S5F and S5G).

It has been reported that lipid storage helps to maintain the integrity of the endoplasmic reticulum (ER) (Giu et al., 2015). We examined the expression of ER-related genes but did not detect a significant change following JMJD6 silencing (Figure S5H). It has also been reported that lipid droplet accumulation decreases the potential for fatty acid oxidation-mediated ROS production in mitochondria and apoptosis (Cheng et al., 2020). We utilized a Seahorse instrument to measure oxygen consumption from fatty acid oxidation (Zhang and Zhang, 2019) in 786-O cells and found that there were more fatty acids metabolized in mitochondria upon DGAT1 and JMJD6 knockdown. This was the case for at least one of the sgRNAs tested (Figure S5I-L). For the other sgRNA (sgDGATI #2, sgJMJD6 #4), we observed a modest increase in fatty acid oxidation that did not achieve statistical significance. We measured ROS levels in mitochondria by applying the MitoSOX™ Red reagent. The results showed that mROS (mitochondrial ROS) levels were increased in both DGAT1 and JMJD6 knockdown cells (Figure S5M-P). Further, increased cell apoptosis was also observed in both DGAT1 and JMJD6 knockdown cells (Figure S5G-T). We further applied NAC (a well-known scavenger of ROS) to perform rescue experiments on both 2D and 3D. The results showed that NAC could rescue the effect of DGAT inhibitor on mROS (Figure S5U and S5V) as well as decreased 2D and 3D colony formation caused by DGAT1i (Figure S5W-Z). In summary, we established that DGAT1 is a critical mediator of the effect of JMJD6 on lipid droplet formation and cell growth in ccRCC.

DGAT1 is Essential for ccRCC Tumor Growth and DGAT1 Inhibition Suppresses ccRCC Development

Next, we treated ccRCC cells with the DGAT1 inhibitor A922500 and found that A922500 inhibited 3D colony formation in a dose-dependent manner (Figure 6A and 6B). Interestingly, A922500 did not grossly affect normal HKC growth. Through an orthogonal approach, we also found that A922500 interfered with the effect of JMJD6 on ccRCC cell growth (Figure S6A and S6B). Motivated by this finding, we injected 786-O cells expressing luciferase orthotopically into the kidney. Following confirmation of successful engraftment and stable growth, we treated these mice with either vehicle or 60 mg/kg A922500 (by oral gavage). A922500 significantly decreased tumor formation (Figure 6C and 6D). A922500 did not display gross toxicity as indicated by relatively stable mouse weights (Figure S6C).

Upon necropsy, we also found that A922500 treatment led to decreased tumor size and tumor weight (Figure S6D; Figure 6E). In addition, we observed that A922500 decreased lung metastasis (Figure S6E and S6F).

To further verify the role of DGAT1 in maintaining ccRCC tumor growth *in vitro* and *in vivo*, we generated a doxycycline-inducible sh*DGAT1* 786-O cell line. After adding doxycycline, we observed effective DGAT1 knockdown at the protein level (Figure 6F), and decreased cell proliferation, 2D colony formation, and 3D soft agar formation (Figure 6G-I). We further labeled doxycycline-inducible *DGAT1* shRNA (or control shRNA) 786-O cells with firefly luciferase and injected them orthotopically into the kidney of NSG mice. We observed decreased kidney tumor growth upon *DGAT1* knockdown (Figure 6J and 6K). Concordantly, *DGAT1* knockdown decreased tumor weight and tumor size at necropsy (Figure 6L and 6M). In addition, knockdown of DGAT1 decreased lung metastasis (Figure 6N-P).

Finally, we utilized our SPORE RCC tumorgraft platform (Elias et al., 2021; Pavia-Jimenez et al., 2014), and classified PDXs by their basal *DGAT1* expression as quantified by RNA-seq (Figure S6G). We selected one exemplar PDX line (XP745) with high *DGAT1* expression and treated it with A922500. As determined by MRI imaging, A922500 inhibited tumorgraft growth (Figure S6H). This effect was further confirmed by tumor size and weight measurements upon necropsy (Figure S6I and S6J). It is also worth noting that DGAT1 knockout mice are viable, fertile and normal in size (Smith et al., 2000). In addition, these mice do not display gross physical or behavioral abnormalities (Smith et al., 2000). Therefore, targeting ccRCC with DGAT1 inhibitor may be feasible. In summary, pharmacological inhibition or genetic depletion of *DGAT1* decreased ccRCC progression *in vivo*.

DISCUSSION

In this study, we implicate *JMJD6* as an oncogene in ccRCC. *JMJD6*, which was identified through an unbiased siRNA screen of 2-OG dependent enzymes, is required for ccRCC tumor growth in *in vitro* and *in vivo*. Interestingly, the effect of JMJD6 on ccRCC growth is independent of its catalytic activity. By performing genomic analyses for JMJD6 and histone post-translational modifications, we found that JMJD6 occupies target gene promoters and potentially transactivates downstream target genes in ccRCC. Our integrated analyses of ChIP-seq, RNA-seq and patient outcome data led to the identification of *DGAT1* as a key JMJD6 effector implicated in lipid storage and tumorigenesis in ccRCC (Figure 6Q). Therapeutically, DGAT1 inhibition by A922500 inhibited ccRCC tumor growth and spontaneous lung metastasis. Thus, our study, for the first time, identifies the JMJD6-DGAT1 oncogenic signaling axis as a therapeutic target in ccRCC.

JMJD6 was originally found to be a histone arginine demethylase for H3R2 and H4R3 (Chang et al., 2007). Shortly afterwards, JMJD6 was found to catalyze lysine hydroxylation on U2AF65, a protein associated with RNA splicing (Webby et al., 2009), and has since been thought to participate in these two main processes. The difference in the interpretation for the role of JMJD6 in these enzymatic reaction remains to be determined and solidified.

The role of JMJD6 in cancer has been explored in several different cancer types, where it has been implicated in protein hydroxylation in colon cancer (Wang et al., 2014), and protein demethylation (Aprelikova et al., 2016) and tyrosine kinase phosphorylation (Liu et al., 2019) in breast cancer, and protein complex partner in neuroblastoma (Wong et al., 2019), etc. We show here that JMJD6 bound target gene promoter regions with H3K4me3 and H3K27ac and activated *DGAT1* gene expression. More than 30% of genes in higher eukaryotes are regulated by promoter-proximal pausing of pol II (Adelman and Lis, 2012). In a previous study, JMJD6 and Brd4 were found to cooperatively bind distal enhancers defined as anti-pause enhancers (A-PEs). JMJD6 displayed demethylation activity towards H4R3me2 and methyl groups in the 7SK snRNA cap, thereby promoting transcriptional pause release and elongation (Liu et al., 2013). However, given the literature suggesting that JMJD6 may not act as an arginine demethylase, it is unclear whether this transcriptional pause and release model can sufficiently account for the mechanism by which JMJD6 regulates transcription and gene expression. In our manuscript, we propose that JMJD6 binds RBM39, which may promote *DGAT1* gene expression. Recent research show that RBM39 may bind with MLL family members to promote gene expression (Puvvula et al., 2021). However, we did not observe JMJD6 binding with selective MLL family members in ccRCC. Therefore, it is likely that RBM39 may not bind with these methyltransferases in our setting. Further research needs to be performed with regarding to the potential role of MLL family members on JMJD6-RMB39 signaling axis in ccRCC.

DGAT1 is an important TG synthase and is required for storage of intracellular lipids. Upstream regulators of *DGAT1* in cancer remain largely unknown, but our unbiased siRNA screen coupled with integrated genomic analyses pinpointed JMJD6 as a critical transcriptional regulator of *DGAT1*. Here, for the first time, we examined the potential therapeutic efficacy of the DGAT1 inhibitor A922500 in ccRCC. By treating tumor-bearing mice with A922500, we observed decreased tumor growth over time. We also observed a similar phenotype by genetic depletion of *DGAT1* with inducible shRNAs *in vivo*. Importantly, the effect was specific for tumor cells and normal renal epithelial cells were spared. It is also worth noting that DGAT1 knockout mice are viable, fertile and normal in size (Smith et al., 2000). In addition, these mice do not display gross physical or behavioral abnormalities (Smith et al., 2000). Therefore, targeting ccRCC with DGAT1 inhibitor may be feasible. Future studies will further optimize the dosage and delivery of DGAT1 inhibitors in patient-derived xenografts. In addition, we will examine whether *DGAT1* expression can serve as a biomarker to stratify ccRCC patients for potential DGAT1 inhibitor treatment in the clinical setting.

Limitations of the Study

The detailed mechanism by which JMJD6 regulates DGAT1 gene expression remains to be fully elucidated. Our study still lacks the detailed mechanism on how JMJD6 would affect H3K4me3 occupancy on some of target gene promoters. At this time, the role of RBM39 in JMJD6-DGAT1 signaling axis awaits further characterization and it is unclear whether this involves the effect of RBM39 on regulating RNA splicing. In addition, further studies are needed to examine the efficacy and toxicity of DGAT1 inhibition in a large cohort of kidney cancer PDXs and relevant kidney cancer mouse models.

STAR★ METHODS

RESOURCE AVAILABILITY

Lead contact—Further information and requests for resources and reagents should be directed to and will be fulfilled by the Lead Contact, Qing Zhang (qing.zhang@utsouthwestern.edu).

Materials availability—All materials generated in this study are available from the Lead Contact with a completed Materials Transfer Agreement.

Data and code availability—ChIP-seq and RNA-seq data have been deposited at GEO under accession number GSE182888 and are publicly available as of the date of publication. Accession numbers are also listed in the key resources table. Original western blot and crystal violet images have been deposited at Mendeley and are publicly available as of the date of publication. The DOI is listed in the key resources table. Mass spectrometry data are presented in the table S2. Microscopy data reported in this paper will be shared by the lead contact upon request.

This paper does not report original code.

Any additional information required to reanalyze the data reported in this paper is available from the lead contact upon request.

EXPERIMENTAL MODEL AND SUBJECT DETAILS

Cell lines—UMRC2, UMRC6, 786-O, 498, HKC, and 293T cells were cultured in Dulbecco's Modified Eagle's Medium (DMEM) medium supplemented with 10% fetal bovine serum (FBS) and 1% penicillin/streptomycin, incubated in a 5% CO2 humidified incubator at 37°C. All cells were used for experiments within 10-20 passages from thawing, and they were mycoplasma-free according to a mycoplasma detection kit (Lonza, LT07–218) or mycoplasma elimination reagent-plasmocin (Invivogen, ant-mpt).

Orthotopic Tumor Xenograft—For xenograft studies, six-week-old NSG (Jackson lab, male: female=2:1 for gene knockdown model, but females were used only in inhibitor treatment model due to toxicity to male mice) and luciferase reporter cell lines were used. Briefly, $1\chi10^6$ 786-O cells expressing control/tet-on JMJD6 shRNA, or 5×10^5 786-O cells expressing control/tet-on DGAT1 shRNA or 7.5×10^5 786-O parental cells were resuspended in 20 μL Matrigel that was diluted with medium without PBS by 1:1, and then injected orthotopically into the left kidney of each mouse as described previously (Zhang et al., 2018). SPECTRAL AMI-HTX imaging system was applied to monitor tumor growth *in vivo*. Luciferin (15 mg/mL) was applied by intraperitoneal injection (IP) to monitor the mice weekly, and the luciferin signal is stably increased at week 4 compared to the previous week, followed by further treatment. For inducible JMJD6 and DGAT1 shRNA, mice were fed Purina rodent chow doxycycline. For DGAT1 inhibitor treatment, mice were randomly divided into two groups (Ctrl and DGAT1i), the DGAT1i group mice were treated with DGAT1 inhibitor A922500 (60 mg/kg/day, formulated with 1% Tween80 in PBS) by oral gavage while the ctrl group mice were treated with vehicle. After 5-8 weeks of treatment,

mice were euthanized. Tumors were taken out and weighed, the weight of tumor was calculated by subtracting the weight of left tumor kidney from the weight of right normal kidney. Lungs were taken out followed by *ex vivo* imaging in 24-well plates with 300 μg/mL luciferin solution. For the PDX model, it was performed under the guidance of the human renal cell carcinoma tumorgraft platform for preclinical drug testing at UTSW (Pavia-Jimenez et al., 2014). Briefly, 2 pieces of ~2 mm PDX sample was implanted in the left kidney of each mouse. After one week, the size of the tumors (zero point) was measured by using MRI, and then treatment with DGAT1 inhibitor A922500 began. After three weeks, we used MRI to image the tumors again. Tumors were excised and subsequent data collection was the same as described above. All animal experiments met the requirements of National Institutes of Health guidelines and were approved by the Institutional Animal Care and Use Committee (IACUC) in the University of Texas Southwestern Medical Center (Protocol # 2019-102794).

METHOD DETAILS

Cell Proliferation and Colony Formation Assay—For cell proliferation assays, specific numbers of cells (~800-1000 cells/well) were seeded in 96-well plates in DMEM medium and changed with fresh medium every 2 days. At indicated time points, the cells were cultured in 100 μl fresh growth medium supplemented with 10 μl MTS reagents (Abcam, ab197010), following by incubation at 37°C for ~1hrs. OD absorbance values were measured at 490 nm using the BioTek plate reader. For Incucyte cell growth curves, cells (~800-1000 cells/well) were seeded in 96-well plates in DMEM medium. Plates were incubated at the Incucyte® S3 incubator and changed with fresh medium every 2 days. We applied the IncuCyte S3 Plate Map Editor 2018B to set profile information, and applied IncuCyte S3 2018B software to monitor the cells by taking images for each well at indicated points and collect/analyze corresponding data. For crystal violet staining, cells were seeded in 6-well plates (2000 cells/well), after the cells reach a specific density visually, they were stained with 0.5% crystal violet for 1 h. For the soft agar colony formation assay, specific numbers of cells (10,000 cells for HKC, 20,000 cells for UMRC2/UMRC6/786-O, and 30,000 cells for A498) were applied to prepare the upper layer in 6-well plates, after 2-6 weeks, 100 μg/mL iodonitrotetrazoliuim chloride solution was used to stain cell colonies. Detailed steps were referred to previous paper (Zhang et al., 2018). Colony quantification was performed by using ImageJ software.

Real-Time PCR—Total RNA was extracted by using a RNeasy mini kit, followed by cDNA synthesis using an iScript™ cDNA Synthesis Kit. Real-time PCR was conducted in 384-well optical reaction plates using the CFX384 Real-Time PCR System (Bio-Rad). Relative amplicon expression was calculated using the $2^{-\Delta\Delta Ct}$ method. The sequence of Real-time qPCR primers can be found in table S5.

Virus Infection—As to lentiviral plasmids, 293T cells were used for virus production. Briefly, ~80% confluency of 293T cells were applied to transfect with helper plasmids psPAX2/pMD2.G and lenti-viral vector plasmids in 6-well plates. After incubation overnight, cells were replaced with 1.5 ml fresh medium and virus was collected after one day, cells were changed with fresh medium again for a 2nd collection after another day

of culturing. 0.45 μm filters were used to filter the virus. ccRCC cell lines were seeded in 6-well plates to be 30-50% confluent at infection, 200 μl virus/well was applied, and 6-8 μg/mL polybrene was included to increase efficiency during the infection. Media were changed after 12-24 h infection, then the cells underwent appropriate antibiotic selection after more than 24 h incubation (puromycin 2 μg/mL for shRNA/sgRNA, G418 800 μg/mL for pInducer-JMJD6/CD and pInducer-DNAJB12/IPO13, hygromycin 200 μg/mL for UBCp-JMJD6, and blasticidin 10 μg/mL for pLX-DGAT1 and pLenti6.3-MFSD3). For lipid droplet study, the time of marker selection should be strictly controlled based on cell line types. Detailed information of the lentiviral plasmids used in this study are as below: pInducer-JMJD6/CD (H187A/D189A) were constructed using gateway reaction based on pDONR 223 and pInducer20, pInducer-DNAJB12/IPO13 were constructed using pInducer20 based on LR reaction. JMJD6 sgRNAs were constructed using lentiCRISPR v2, and JMJD6 tet-on shRNA was constructed using Tet-pLKO-puro, corresponding target sequence can be found in KEY RESOURCES TABLE. DGAT1 sgRNA2 and shRNAs/tet-on shRNA were obtained from Dr. Deliang Guo lab (Cheng et al., 2020).

siRNA Transfection—UMRC2 and A498 cells were seeded in 6-well plates to be 60~70% confluent while 786-O cells were 40~50% confluent at transfection, followed by transfection using the invitrogen™ lipofectamine™ RNAiMAX reagent (8 μl RNAiMAX and 5 μl 20 μM siRNA were used per well), and media were changed after 12 h transfection. Cells were incubated for > 48 h at 37°C then used to perform downstream experiments (immunoblots, cell proliferation assay, and soft agar colony formation assay). Non-targeting siRNA was used as control. The sequence of siRNA used in this study can be found in table S1 and Key Resources Table.

Lipid Droplet Staining and Quantification—Lipid droplet staining was performed as described previously (Melo et al., 2011). Briefly, after culturing and treatment, cells were fixed in 4% paraformaldehyde (PFA) for 15 min, washed twice with PBS, then were stained with BODIPY™ 493/503 (1 μM) or HCS LipidTOX™ Red (1:200) for 1 h. Cells were then again washed twice with PBS, followed by DAPI or Hoechst 33342 (1:1000) incubation for 5 min, and mounted on slides. Lipid droplets were visualized using a Revolve fluorescence microscope (Echo). Six images were taken in total/group, and lipid droplets levels were quantified by using the ImageJ software (Fiji). Average integrated density (IntDen) per cell in each image was used to plot the graph.

Triglyceride Detection—UMRC2, 786-O and HKC cells were seeded in 10 cm dishes to be 80-90% confluent, then treated with DMSO or DGAT1 inhibitor A922500 (20 μM) for 24 h. Cells were then collected to measure triglyceride levels according to manufacturer's instructions using the triglyceride quantification colorimetric/fluorometric kit. Briefly, cells (1×10^7) were homogenized in 1 mL solution of 5% Nonidet P 40 Substitute, followed by 95°C heating for 4 mins twice. Then, solutions were centrifuged for 2 mins at top speed to remove insoluble material and eluates were diluted 10-fold with water before assay. 2 μl lipase was added to each well followed by incubation for 20 mins at room temperature. Afterwards, the Master Reaction Mix was set up according to the protocol of the kit and the absorbance was measured at 570 nm by using the BioTek plate reader.

Oxygen consumption rate (OCR) measurement—Seahorse XFe24 Analyzer was used. The experimental procedure of OCR measurement was described previously (Zhang and Zhang, 2019). Briefly, about 2×10^4 786-O cells were seeded into the XF24 cell culture microplate the day before assay, and the cells were cultured in substrate-limited medium (basal DMEM supplemented with 1% FBS, 0.5 mM Carnitine, 0.5 mM Glucose and 1.0 mM GlutaMAX) overnight. In the meantime, calibrant was added into the bottom layer of the XFe24 sensor cartridges (1 ml per well), then it was sealed by using plastic wrap and incubated at 37°C incubator overnight. The next morning, the media were changed with freshly prepared and prewarmed FAO assay buffer (450 μl per well) supplemented with 5 mM HEPES, 0.5 mM Carnitine and 2.5 mM Glucose, with pH adjusted to 7.4, and then the microplate was incubated in general 37°C incubator for 20 min. Concurrently, 400 μM fatty acid oxidation inhibitor (ETO) was prepared in FAO buffer and added into the upper layer of the XFe24 sensor cartridges (50 μl per well). The Seahorse XFe24 Analyzer was set up and the sensor cartridges were loaded for calibration. The plates were analyzed according to the manufacturer's instructions. Data was normalized by cell counting for each well.

Flow Cytometry—The apoptosis assay was conducted by using the Biolegend FITC Annexin V Apoptosis Detection Kit with PI (50-403-826, Fisher Scientific) according to the manufacturer's instructions. Culture medium were changed the day before assay. Trypsin without EDTA was used to trypsinize cells. Cells were counted for a cell suspension at $5x10^7$ cells / ml. After FITC Annexin V and PI were added and gently mixed followed by incubation for 15 min at room temperature. Cells were analyzed at the Flow Cytometry Core Facility in the University of Texas Southwestern medical center.

Mitochondrial Superoxide Detection—The mitochondrial reactive oxygen species (ROS) level was measured by applying the MitoSOX™ Red Mitochondrial Superoxide Indicator according to the manufacturer's instructions. Briefly, cells were seeded on the coverslips the day before measuring to allow cells to adhere. The next day, MitoSOX™ Red reagent was applied the to the cells and incubated for 10 minutes at 37 °C. Cells were gently washed with PBS three times, and incubated with Hoechst for 5 minutes, then mounted and imaged using a Revolve fluorescence microscope (Echo).

Immunohistochemistry (IHC)—A rabbit polyclonal antibody against JMJD6 (Cell Signaling Technology, 60602S) was used for IHC staining. IHC was carried out in the Bond Autostainer (Leica Microsystems Inc.; Norwell MA). Briefly, after dewaxing and hydrating, antigen retrieval was performed for 20 min at 100°C in EnVision FLEX Target Retrieval Solution (Low pH). Slides were incubated with JMJD6 (1:1000) primary antibody for 20 min, followed by secondary antibody incubation. Antibody detection was conducted using the BOND Intense R detection system with ImmPress Horseradish Peroxidase anti-rabbit, then stained slides were dehydrated and cover slipped. Positive and negative controls were also included in this experiment. For slides analysis, pathologist Liwei Jia from department of Pathology at UT Southwestern Medical Center was responsible for detailed pathological analysis while pathologist Payal Kapur was responsible for *H*-score analysis, detailed analysis results are showed in table S3. For images taken, stained slides were digitally scanned at 40x magnification using NanoZoomer S60 Digital slide scanner C13210-01 at

UTSW Whole Brain Microscopy Facility, and representative images showed are at 20x combined with 40x magnification.

Western Blotting—EBC buffer (120 mM NaCl, 0.1 mM EDTA, 50mM Tris-HCl pH8.0, 0.5% NP40 and 10% glycerol) supplemented with protease inhibitor cocktail (Roche) and phosphoSTOP tablets (Roche) was used as lysis buffer. Tissue samples were homogenized by using TissueRuptor II (QIAGEN) while cell samples were lysed directly in EBC buffer followed by centrifuging at 14000 rpm, 4°C for 10 min using a benchtop centrifuge (MIKRO 200R). Cell lysate protein concentration was measured by Bradford assay, and further equal adjusted. The same amount of protein was loaded and resolved by SDS-PAGE. For clinical tissue samples, Ponceau S staining was performed post-transfer by applying ponceau stain (0.1% dye and 5% of acetic acid) for 5 min, and images were captured by using the Epson Scanner. Normally after transferring and blocking, the NC membranes were incubated with primary antibodies (all antibodies were diluted at 1:1000) overnight and incubated with secondary antibodies (1:5000 dilution) the next day. The membranes were incubated with chemiluminescent substrates ECL or SuperSignal™ West Femto maximum sensitivity substrate, and protein bands were acquired by using the ChemiDoc Imaging System (Bio-Rad).

Immunoprecipitation and Mass Spectrometry—Prepare whole-cell lysates using EBC buffer supplemented with phosphatase inhibitor and protease inhibitor. Measure protein concentration by Bio-Rad Protein Assay Dye and equal the amount of protein incubating with primary antibodies. Specifically, cell lysates were incubated with anti-HA affinity matrix overnight while incubated with anti-FLAG® M2 affinity gel just for 4h. For general immunoprecipitation, agarose beads binding with proteins were washed three times (10min rotation at 4°C/time and centrifugation at 2000rpm for 2min), then use 3x loading to denature protein at 95~100°C for 10min. For mass spectrometry analysis, 8M urea was used to elute the proteins on the agarose beads. Take 5-10% final elution for diagnostic silver staining, while apply TCA precipitation for all the remaining elution. Send the air-dried pellet for further mass spectrometry analysis.

Human ccRCC tumors—Cell lysates generated from defined ccRCC patient tissues with WT VHL or loss of VHL were obtained from UNCseq projects as described previously (Zhang et al., 2018) and was previously approved by the University of North Carolina at Chapel Hill Institutional Review Board (IRB). The fresh-frozen human paired (ccRCC and adjacent normal tissue) samples were obtained from UTSW and the sample related studies have been approved by the UT Southwestern Institutional Review Boards (IRBs).

QUANTIFICATION AND STATISTICAL ANALYSIS

RNA-seq Analysis—Total RNA was extracted from 786-O cells (in triplicate) post 72 hours infected with control or JMJD6 sgRNA2/4 using the RNeasy® Mini Kit, and RNase-Free DNase Set was applied for DNase digestion during RNA purification. Library preparation, quality control and sequencing were performed by Novogene company, the reads were analyzed as described previously (Liu et al., 2020). Briefly, reads were filtered for adaptor contamination using cutadapt such that we can get a quality score > 20 for at

least 90% of bases of each read. Reads were aligned to the reference genome (hg19) using the STAR version 2.5.2b retaining only primary alignments. Then the reads overlapping blacklisted regions of the genome were removed. Transcript abundance was estimated using salmon and differential expression was detected using DESeq2. The RNA-seq data were deposited in GEO under the accession number GSE182888. The clinical RNA-seq data was obtained from Dr. Roy Elias at Internal Medicine of the UT Southwestern Medical Center. These RNA-seq data were deposited in EGA under the accession number EGAS00001005516. Comparison analysis between two set of data and Pearson analysis between two genes (JMJD6-DGAT1/MFSD3/IPO13/DNAJB12/ZSWIM8), as well as graph plotting were performed using Prism 9.0.

ChIP-seq and Integrated Analysis—ChIP was performed on 786-O cells with anti-JMJD6 and anti-H3K4me3 antibody. Briefly, samples were cross-linked with 1% formaldehyde on a shaker for 10 min, followed by adding 125 mM glycine to quench unreacted formaldehyde. Samples were collected by centrifuging at 1500 × g, 4°C for 10 min (50 ml tube, 20 150 mm dishes per sample), followed by lysis and sonication (in 5 ml lysis buffer with 1 ml 0.5 mm glass beads; 30 s on 30 s off/cycle, 50 cycles in total). Meanwhile, dynabeads were incubated with JMJD6 or H3K4me3 antibody at 4°C (100 μl beads using 10 μg antibody), rotating overnight. The sonicated samples were then incubated with antibody-bound dynabeads overnight at 4°C. Beads were washed 8 times by applying a magnetic stand, then spun to collect samples, and eluted 30 min at 65°C, followed by reversing crosslinks at 65°C overnight. RNA was digested using RNase at 37°C for 1 h, and protein was digested using Proteinase K at 55°C for 2 h. DNA was purified using Qiagen PCR purification kit. DNA libraries were prepared using NEBNext® Ultra™ II DNA Library Prep Kit for Illumina® combined with NEBNext Multiplex Oligos for Illumina according to manufacturer's instructions. The quality of prepared DNA library was checked by applying High Sensitivity D1000 Reagents and corresponding ScreenTape (5067-5584/5585, Agilent Technologies). Briefly, 2 μl sample buffer and 2 μl ladder or DNA library sample were applied in optical tube strips (401428, Agilent Technologies), mixed thoroughly for 1 min by using a vortex mixer followed by briefly centrifugation. Then, these samplers and the ScreenTape were loaded into the Agilent 4200 TapeStation machine followed by measurement. After the band size was analyzed to make sure the size of DNA is appropriate (300~500bp), the DNA was sent for sequencing at the CRI's Sequencing Facility at UT Southwestern. The reads were processed as previously described (Liu et al., 2020; Zhang et al., 2018). The JMJD6 ChIP-seq data was deposited to GEO under the accession number GSE182888. The histone modification (except H3K4me3) ChIP-seq data were obtained from GSE86095, and HIF ChIP-seq data were obtained from GSE98012. Prognostic value of genes was analyzed as previously described (Zhang et al., 2018). Briefly, we used software R (R package survival_2.40-1) to perform univariate Kaplan–Meier analysis using the Cox–Mantel log-rank test. Patients were stratified into 2 or 3 equal-sized groups based on rank order of gene expression, and overall survival was used as an endpoint. Important JMJD6 direct target genes in ccRCC were identified by applying the criteria as below: 1. for RNA-seq data, differential expression adj$P < 0.05$; 2. for TCGA data, C-index > 0.5, Cox P value < 0.05, and Cox hazard ratio is higher than 1; 3. for ChIP-seq data, JMJD6 and H3K4me3 binding peaks in the promoter regions (TSS +/− 5 kb).

For ChIPs that only aimed for ChIP-PCR, we applied the SimpleChIP® Enzymatic Chromatin IP Kit to perform anti-pol II, anti-H3K4me3 or anti-HA tag antibody ChIP in 786-O cells. The sequence of ChIP-qPCR primers can be found in table S6. The data obtained were analyzed using the following formula to indicate the abundance of proteins enriched at the gene promoters: percent input = $100\% \times 2^{(\text{CT input sample} - \text{CT IP sample})}$.

Statistical Analysis—The experimental data were presented as mean ± SEM. Statistical analysis was carried out using Prism 9.0 (GraphPad Software), unpaired/paired T-test and Pearson Correlation were applied to analyze two sets of data, while one-way ANOVA followed by a post hoc Dunnett-t-test or a post hoc Bonferroni–t-test was used to perform multiple comparisons. For statistical significance, *, **, *** and **** denote *P* value of < 0.05, 0.01, 0.001 and 0.0001 respectively, and n.s. means no significance.

Supplementary Material

Refer to Web version on PubMed Central for supplementary material.

ACKNOWLEDGMENTS

This work was partially supported by Cancer Prevention and Research Institute of Texas (CPRIT) (Q. Zhang, CPRIT, RR190058) Department of Defense Kidney Cancer Research Program Idea Development Award (W81XWH1910813), National Cancer Institute (Q. Zhang, R01CA211732, J.B, P50CA196516). D.N. is supported by R37CA226771 from the NCI, a Welch Foundation Award (I-1879), and a UT Presidential Scholar Award. We thank Dr. Jian Xu and Sequencing Facility of Children's Medical Center Research Institute (CRI) at UT Southwestern for their helps. We thank the UTSW Tissue Management Shared Resource Center at the Simmons Comprehensive Cancer Center which is supported in part by the National Cancer Institute under award number P30 CA142543. We acknowledge the assistance of the Preclinical Radiation Core Facility which is supported by CPRIT (RP180770). We thank Dr. Ralph DeBerardinis's guidance. We thank Dr. Lei Bao and Prof. Weibo Luo for ChIP technical support and MLL-C antibody sharing. We thank Dr. Xiang Cheng and Prof. Deliang Guo for providing DGAT1 shRNA/sgRNA plasmids, and we thank Dr. Jaeil Han and Prof. Joshua Mendell for providing ZSWIM8 plasmid. We thank Dr. Sabine Lang and Prof. Qin Yan for providing MLLs antibodies. We also want to thank kidney cancer patients for donating their tissues for this study.

REFERENCES

Adelman K, and Lis JT (2012). Promoter-proximal pausing of RNA polymerase II: emerging roles in metazoans. Nat Rev Genet 13, 720–731. [PubMed: 22986266]

Aprelikova O, Chen K, El Touny LH, Brignatz-Guittard C, Han J, Qiu T, Yang HH, Lee MP, Zhu M, and Green JE (2016). The epigenetic modifier JMJD6 is amplified in mammary tumors and cooperates with c-Myc to enhance cellular transformation, tumor progression, and metastasis. Clin Epigenetics 8, 38. [PubMed: 27081402]

Barak T, Ristori E, Ercan-Sencicek AG, Miyagishima DF, Nelson-Williams C, Dong W, Jin SC, Prendergast A, Armero W, Henegariu O, et al. (2021). PPIL4 is essential for brain angiogenesis and implicated in intracranial aneurysms in humans. Nat Med 27, 2165–2175. [PubMed: 34887573]

Bottger A, Islam MS, Chowdhury R, Schofield CJ, and Wolf A (2015). The oxygenase Jmjd6--a case study in conflicting assignments. Biochem J 468, 191–202. [PubMed: 25997831]

Cancer Genome Atlas Research, N. (2013). Comprehensive molecular characterization of clear cell renal cell carcinoma. Nature 499, 43–49. [PubMed: 23792563]

Chang B, Chen Y, Zhao Y, and Bruick RK (2007). JMJD6 is a histone arginine demethylase. Science 318, 444–447. [PubMed: 17947579]

Chen D, Maruschke M, Hakenberg O, Zimmermann W, Stief CG, and Buchner A (2017). TOP2A, HELLS, ATAD2, and TET3 Are Novel Prognostic Markers in Renal Cell Carcinoma. Urology 102, 265 e261–265 e267.

Chen W, Hill H, Christie A, Kim MS, Holloman E, Pavia-Jimenez A, Homayoun F, Ma Y, Patel N, Yell P, et al. (2016). Targeting Renal Cell Carcinoma with a HIF-2 antagonist. Nature.

Cheng X, Geng F, Pan M, Wu X, Zhong Y, Wang C, Tian Z, Cheng C, Zhang R, Puduvalli V, et al. (2020). Targeting DGAT1 Ameliorates Glioblastoma by Increasing Fat Catabolism and Oxidative Stress. Cell Metab 32, 229–242 e228. [PubMed: 32559414]

Cho H, Du X, Rizzi JP, Liberzon E, Chakraborty AA, Gao W, Carvo I, Signoretti S, Bruick R, Josey JA, et al. (2016). On-Target Efficacy of a HIF2alpha Antagonist in Preclinical Kidney Cancer Models. Nature.

Cloos PA, Christensen J, Agger K, and Helin K (2008). Erasing the methyl mark: histone demethylases at the center of cellular differentiation and disease. Genes & development 22, 1115–1140. [PubMed: 18451103]

Dowhan DH, Hong EP, Auboeuf D, Dennis AP, Wilson MM, Berget SM, and O'Malley BW (2005). Steroid hormone receptor coactivation and alternative RNA splicing by U2AF65-related proteins CAPERalpha and CAPERbeta. Mol Cell 17, 429–439. [PubMed: 15694343]

Elias R, Tcheuyap VT, Kaushik AK, Singla N, Gao M, Reig Torras O, Christie A, Mulgaonkar A, Woolford L, Stevens C, et al. (2021). A renal cell carcinoma tumorgraft platform to advance precision medicine. Cell Rep 37, 110055. [PubMed: 34818533]

Fages J, Chailleux C, Humbert J, Jang SM, Loehr J, Lambert JP, Cote J, Trouche D, and Canitrot Y (2020). JMJD6 participates in the maintenance of ribosomal DNA integrity in response to DNA damage. PLoS Genet 16, e1008511. [PubMed: 32598339]

Fedchenko N, and Reifenrath J (2014). Different approaches for interpretation and reporting of immunohistochemistry analysis results in the bone tissue - a review. Diagn Pathol 9, 221. [PubMed: 25432701]

Godwin JL, Zibelman M, Plimack ER, and Geynisman DM (2014). Immune checkpoint blockade as a novel immunotherapeutic strategy for renal cell carcinoma: a review of clinical trials. Discovery medicine 18, 341–350. [PubMed: 25549705]

Han J, LaVigne CA, Jones BT, Zhang H, Gillett F, and Mendell JT (2020). A ubiquitin ligase mediates target-directed microRNA decay independently of tailing and trimming. Science 370.

Han T, Goralski M, Gaskill N, Capota E, Kim J, Ting TC, Xie Y, Williams NS, and Nijhawan D (2017). Anticancer sulfonamides target splicing by inducing RBM39 degradation via recruitment to DCAF15. Science 356.

Kaelin WG Jr. (2002). Molecular basis of the VHL hereditary cancer syndrome. Nat Rev Cancer 2, 673–682. [PubMed: 12209156]

King AJ, Segreti JA, Larson KJ, Souers AJ, Kym PR, Reilly RM, Zhao G, Mittelstadt SW, and Cox BF (2009). Diacylglycerol acyltransferase 1 inhibition lowers serum triglycerides in the Zucker fatty rat and the hyperlipidemic hamster. J Pharmacol Exp Ther 330, 526–531. [PubMed: 19478132]

Lee JH, Jeon YG, Lee KH, Lee HW, Park J, Jang H, Kang M, Lee HS, Cho HJ, Nam DH, et al. (2017). RNF20 Suppresses Tumorigenesis by Inhibiting the SREBP1c-PTTG1 Axis in Kidney Cancer. Molecular and cellular biology 37.

Liu W, Ma Q, Wong K, Li W, Ohgi K, Zhang J, Aggarwal A, and Rosenfeld MG (2013). Brd4 and JMJD6-associated anti-pause enhancers in regulation of transcriptional pause release. Cell 155, 1581–1595. [PubMed: 24360279]

Liu X, Simon JM, Xie H, Hu L, Wang J, Zurlo G, Fan C, Ptacek TS, Herring L, Tan X, et al. (2020). Genome-wide Screening Identifies SFMBT1 as an Oncogenic Driver in Cancer with VHL Loss. Mol Cell 77, 1294–1306 e1295. [PubMed: 32023483]

Liu Y, Long YH, Wang SQ, Zhang YY, Li YF, Mi JS, Yu CH, Li DY, Zhang JH, and Zhang XJ (2019). JMJD6 regulates histone H2A.X phosphorylation and promotes autophagy in triple-negative breast cancer cells via a novel tyrosine kinase activity. Oncogene 38, 980–997. [PubMed: 30185813]

Loerch S, Maucuer A, Manceau V, Green MR, and Kielkopf CL (2014). Cancer-relevant splicing factor CAPERalpha engages the essential splicing factor SF3b155 in a specific ternary complex. J Biol Chem 289, 17325–17337. [PubMed: 24795046]

Losman JA, and Kaelin WG Jr. (2013). What a difference a hydroxyl makes: mutant IDH, (R)-2-hydroxyglutarate, and cancer. Genes & development 27, 836–852. [PubMed: 23630074]

Melo RC, D'Avila H, Bozza PT, and Weller PF (2011). Imaging lipid bodies within leukocytes with different light microscopy techniques. Methods Mol Biol 689, 149–161. [PubMed: 21153791]

Miller TE, Liau BB, Wallace LC, Morton AR, Xie Q, Dixit D, Factor DC, Kim LJY, Morrow JJ, Wu Q, et al. (2017). Transcription elongation factors represent in vivo cancer dependencies in glioblastoma. Nature 547, 355–359. [PubMed: 28678782]

Pavia-Jimenez A, Tcheuyap VT, and Brugarolas J (2014). Establishing a human renal cell carcinoma tumorgraft platform for preclinical drug testing. Nat Protoc 9, 1848–1859. [PubMed: 25010905]

Piccolis M, Bond LM, Kampmann M, Pulimeno P, Chitraju C, Jayson CBK, Vaites LP, Boland S, Lai ZW, Gabriel KR, et al. (2019). Probing the Global Cellular Responses to Lipotoxicity Caused by Saturated Fatty Acids. Mol Cell 74, 32–44 e38. [PubMed: 30846318]

Puvvula PK, Yu Y, Sullivan KR, Eyob H, Rosenberg J, Welm A, Huff C, and Moon AM (2021). Inhibiting an RBM39/MLL1 epigenomic regulatory complex with dominant-negative peptides disrupts cancer cell transcription and proliferation. Cell Rep 35, 109156. [PubMed: 34077726]

Qiu B, Ackerman D, Sanchez DJ, Li B, Ochocki JD, Grazioli A, Bobrovnikova-Marjon E, Diehl JA, Keith B, and Simon MC (2015). HIF2alpha-Dependent Lipid Storage Promotes Endoplasmic Reticulum Homeostasis in Clear-Cell Renal Cell Carcinoma. Cancer Discov 5, 652–667. [PubMed: 25829424]

Ran T, Xiao R, Huang Q, Yuan H, Lu T, and Liu W (2019). In Silico Discovery of JMJD6 Inhibitors for Cancer Treatment. ACS Med Chem Lett 10, 1609–1613. [PubMed: 31857835]

Sethi G, Shanmugam MK, and Kumar AP (2017). SREBP-1c as a molecular bridge between lipogenesis and cell cycle progression of clear cell renal carcinoma. Biosci Rep 37.

Siegel RL, Miller KD, and Jemal A (2020). Cancer statistics, 2020. CA: a cancer journal for clinicians 70, 7–30. [PubMed: 31912902]

Sivanand S, Pena-Llopis S, Zhao H, Kucejova B, Spence P, Pavia-Jimenez A, Yamasaki T, McBride DJ, Gillen J, Wolff NC, et al. (2012). A validated tumorgraft model reveals activity of dovitinib against renal cell carcinoma. Sci Transl Med 4, 137ra175.

Smith SJ, Cases S, Jensen DR, Chen HC, Sande E, Tow B, Sanan DA, Raber J, Eckel RH, and Farese RV Jr. (2000). Obesity resistance and multiple mechanisms of triglyceride synthesis in mice lacking Dgat. Nature genetics 25, 87–90. [PubMed: 10802663]

Uehara T, Minoshima Y, Sagane K, Sugi NH, Mitsuhashi KO, Yamamoto N, Kamiyama H, Takahashi K, Kotake Y, Uesugi M, et al. (2017). Selective degradation of splicing factor CAPERalpha by anticancer sulfonamides. Nat Chem Biol 13, 675–680. [PubMed: 28437394]

Varier RA, and Timmers HT (2011). Histone lysine methylation and demethylation pathways in cancer. Biochimica et biophysica acta 1815, 75–89. [PubMed: 20951770]

Walther TC, and Farese RV Jr. (2012). Lipid droplets and cellular lipid metabolism. Annual review of biochemistry 81, 687–714.

Wang F, He L, Huangyang P, Liang J, Si W, Yan R, Han X, Liu S, Gui B, Li W, et al. (2014). JMJD6 promotes colon carcinogenesis through negative regulation of p53 by hydroxylation. PLoS Biol 12, e1001819. [PubMed: 24667498]

Webby CJ, Wolf A, Gromak N, Dreger M, Kramer H, Kessler B, Nielsen ML, Schmitz C, Butler DS, Yates JR 3rd, et al. (2009). Jmjd6 catalyses lysyl-hydroxylation of U2AF65, a protein associated with RNA splicing. Science 325, 90–93. [PubMed: 19574390]

Wong M, Sun Y, Xi Z, Milazzo G, Poulos RC, Bartenhagen C, Bell JL, Mayoh C, Ho N, Tee AE, et al. (2019). JMJD6 is a tumorigenic factor and therapeutic target in neuroblastoma. Nat Commun 10, 3319. [PubMed: 31346162]

Xie D, Li J, Wei S, Qi P, Ji H, Su J, Du N, and Zhang X (2020a). Knockdown of PLOD3 suppresses the malignant progression of renal cell carcinoma via reducing TWIST1 expression. Mol Cell Probes 53, 101608. [PubMed: 32585183]

Xie L, Li H, Zhang L, Ma X, Dang Y, Guo J, Liu J, Ge L, Nan F, Dong H, et al. (2020b). Autophagy-related gene P4HB: a novel diagnosis and prognosis marker for kidney renal clear cell carcinoma. Aging (Albany NY) 12, 1828–1842. [PubMed: 32003756]

Xu F, Guan Y, Xue L, Huang S, Gao K, Yang Z, and Chong T (2020). The effect of a novel glycolysis-related gene signature on progression, prognosis and immune microenvironment of renal cell carcinoma. BMC Cancer 20, 1207. [PubMed: 33287763]

Yao X, Tan J, Lim KJ, Koh J, Ooi WF, Li Z, Huang D, Xing M, Chan YS, Qu JZ, et al. (2017). VHL Deficiency Drives Enhancer Activation of Oncogenes in Clear Cell Renal Cell Carcinoma. Cancer discovery 7, 1284–1305. [PubMed: 28893800]

Zhang C, Lu X, Huang J, He H, Chen L, Liu Y, Wang H, Xu Y, Xing S, Ruan X, et al. (2021). Epigenome screening highlights that JMJD6 confers an epigenetic vulnerability and mediates sunitinib sensitivity in renal cell carcinoma. Clin Transl Med 11, e328. [PubMed: 33634984]

Zhang J, Wu T, Simon J, Takada M, Saito R, Fan C, Liu XD, Jonasch E, Xie L, Chen X, et al. (2018). VHL substrate transcription factor ZHX2 as an oncogenic driver in clear cell renal cell carcinoma. Science 361, 290–295. [PubMed: 30026228]

Zhang J, and Zhang Q (2019). Using Seahorse Machine to Measure OCR and ECAR in Cancer Cells. In Cancer Metabolism: Methods and Protocols, Haznadar M, ed. (New York, NY: Springer New York), pp. 353–363.

Zheng X, Zhai B, Koivunen P, Shin SJ, Lu G, Liu J, Geisen C, Chakraborty AA, Moslehi JJ, Smalley DM, et al. (2014). Prolyl hydroxylation by EglN2 destabilizes FOXO3a by blocking its interaction with the USP9x deubiquitinase. Genes & development 28, 1429–1444. [PubMed: 24990963]

Zhu Z, He A, Lv T, Xu C, Lin L, and Lin J (2019). Overexpression of P4HB is correlated with poor prognosis in human clear cell renal cell carcinoma. Cancer Biomark 26, 431–439. [PubMed: 31640086]

Zurlo G, Liu X, Takada M, Fan C, Simon JM, Ptacek TS, Rodriguez J, von Kriegsheim A, Liu J, Locasale JW, et al. (2019). Prolyl hydroxylase substrate adenylosuccinate lyase is an oncogenic driver in triple negative breast cancer. Nat Commun 10, 5177. [PubMed: 31729379]

Highlights

- An unbiased siRNA screen identifies JMJD6 to be essential for ccRCC 3D growth
- JMJD6 contributes to ccRCC growth in an enzymatically independent manner
- JMJD6 controls LD and ccRCC by interacting with RBM39 to regulate *DGAT1* expression
- DGAT1 inhibitor displays potential therapeutic efficacy in ccRCC

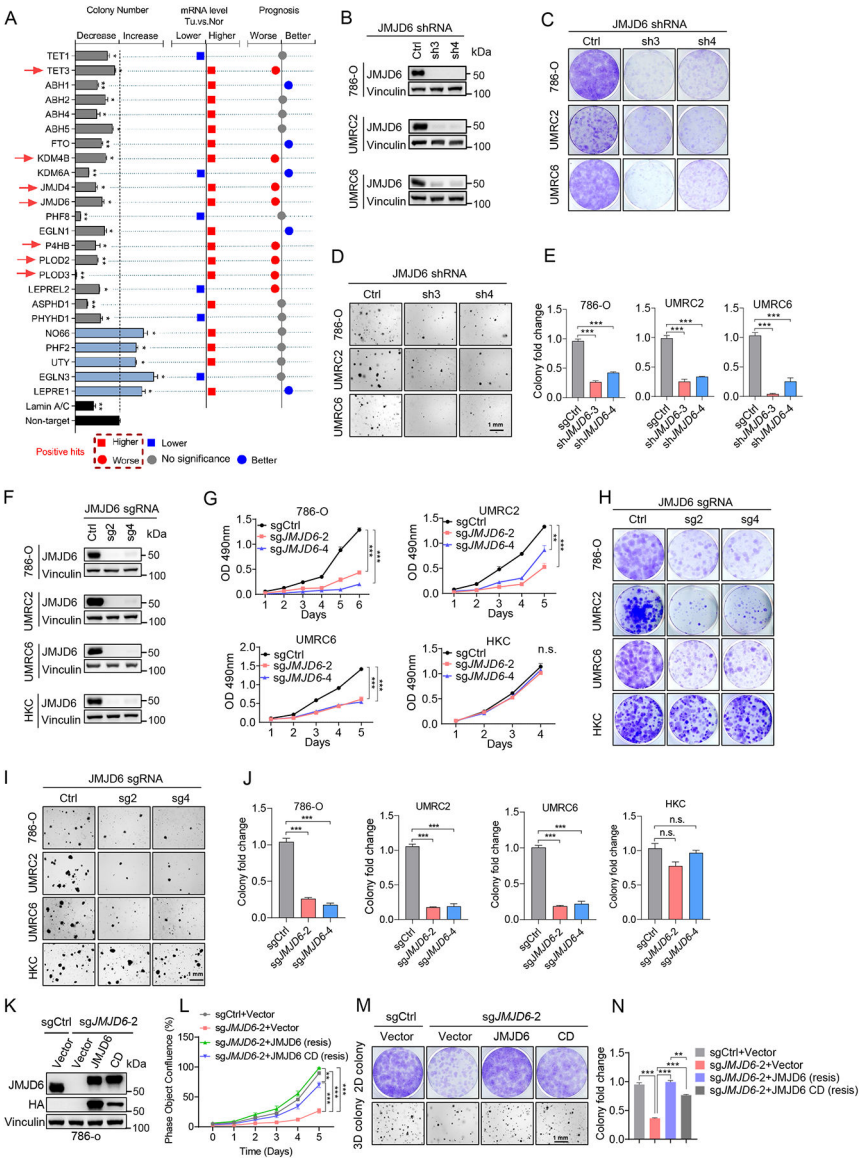

Figure 1. JMJD6 is an Essential Gene for ccRCC Cell Growth

(A) Integration of potential positive hits and mRNA level and prognosis in kidney cancer, hits with decreased colonies & higher mRNA level & worse prognosis were further considered as positive hits.

(B-J) Immunoblotting (B and F), MTS proliferation assays (n=5) (G), 2D colony formation assay (C and H), representative soft agar images (D and I) and corresponding quantification data (n=3) (E and J) in indicated cell lines transduced with shCtrl/sgCtrl, *JMJD6* shRNA3/4 (sh3, sh4) or sgRNA2/4 (sg2, sg4).

(K-N) Immunoblotting (K), incucyte cell proliferation assay (n=5) (L), 2D colony formation assay and representative soft agar images (M), and corresponding quantification data (n=3) (N) in 786-O cells overexpressed with empty vector or HA-*JMJD6* sg2-resistant (JMJD6) or catalytic dead HA-*JMJD6* sg2-resistant (CD) followed by infection with sgCtrl or *JMJD6* sg2.

Error bars represent SEM, two-tailed Student's t-test, *P<0.05, **P<0.01, ***P<0.001. n.s. means no significance.

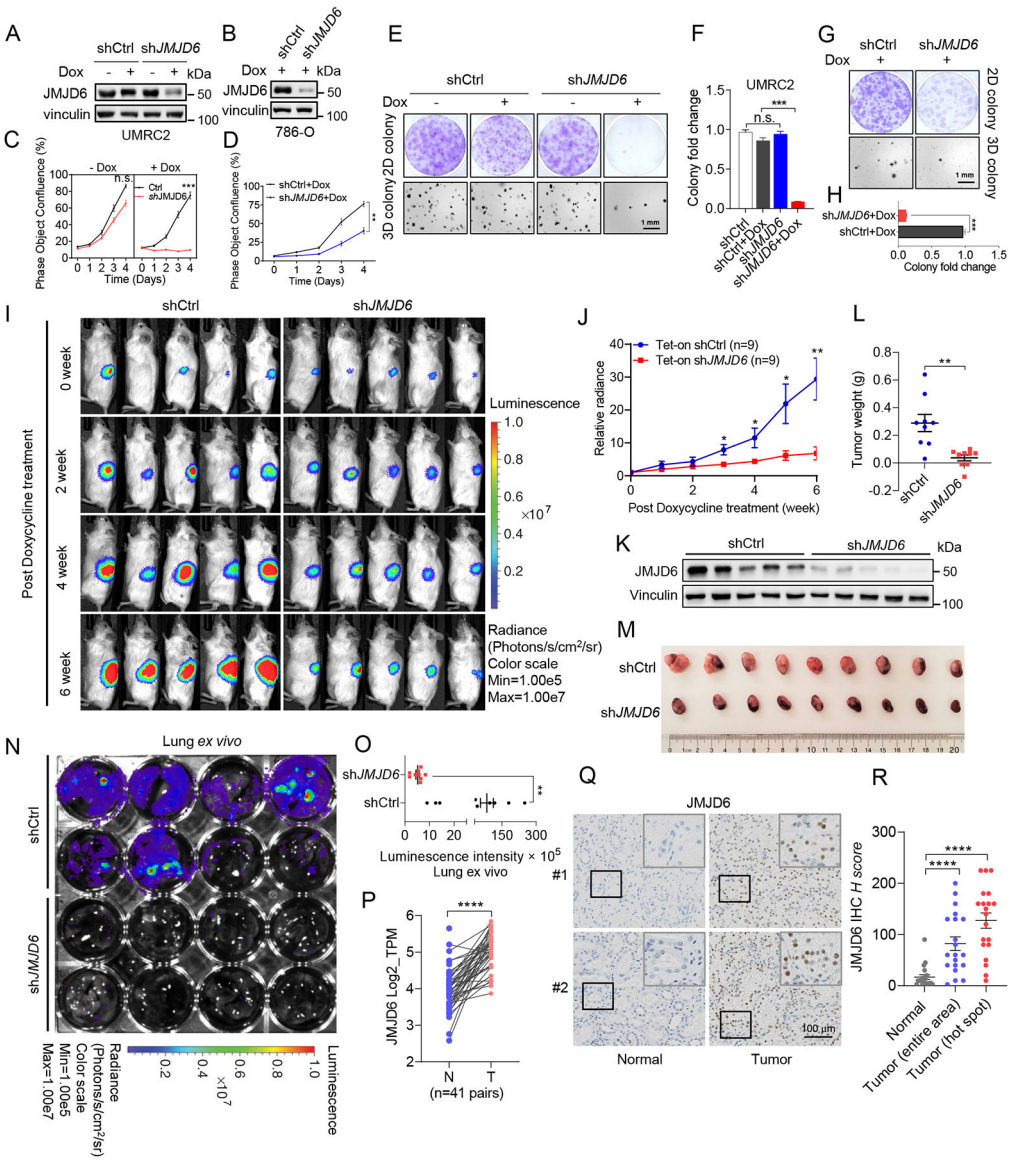

Figure 2. JMJD6 is Required for ccRCC Tumorigenesis *in vivo*

(A-H) Immunoblotting (A and B), incucyte cell proliferation assay (n=5) (C and D), 2D colony formation assay and representative soft agar images (E and G), and corresponding quantification data (n=3) (F and H) in UMRC2 or 786-O luciferase stable cells transduced with teton-control shRNA (shCtrl) or teton-*JMJD6* shRNA4 (sh*JMJD6*) and treated with or without doxycycline as indicated.

(I-O) Representative bioluminescence imaging of mice before (0 week) and 2/4/6 weeks post-doxycycline treatment (I) and corresponding quantification (J), immunoblotting of tumors (K), tumor weight after dissection (L), image of tumors (M), representative lung ex vivo bioluminescence imaging (N) and corresponding quantification (O) from 786-O luciferase stable cell lines that transduced with teton control (shCtrl) or teton-*JMJD6* shRNA4 (sh*JMJD6*) followed by orthotopic injection into the renal sub-capsule of NOD SCID gamma (NSG) mice (n=9).

(P) *JMJD6* mRNA level in paired normal (N) and tumor (T) patient tissues, n=41.
(Q and R) Representative images (Q) and corresponding *H-score* (R) for JMJD6 immunohistochemical (IHC) staining in ccRCC paired patient tissues, n=20.
Error bars represent SEM, two-tailed Student's t-test, **P*<0.05, ***P*<0.01, ****P*<0.001, *****P*<0.0001. n.s. means no significance.

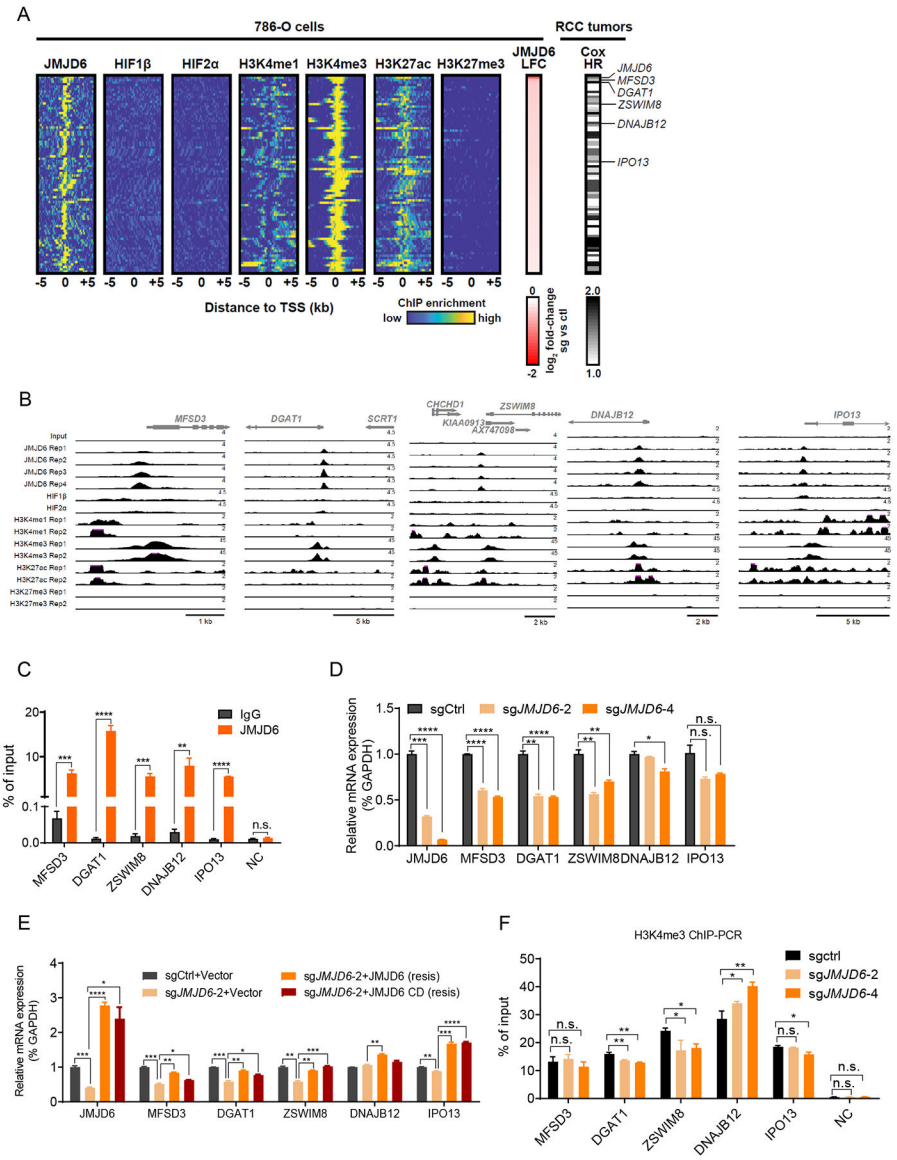

Figure 3. Identification of Critical JMJD6JD6 Target Genes in ccRCC

(A) Integrated analyses of ChIP-seqs (including JMJD6, HIF1β, HIF2α, H3K4me1, H3K4me3, H3K27ac and H3K27me3), log2 fold change (LFC) for JMJD6 RNA-seq with two different sgRNAs, and RCC patient prognosis (Cox HR value). Critical target genes were marked on the right.

(B) ChIP-seq binding peaks on *MFSD3/DGAT1/ZSWIM8/JMJD6/DNAJB12/IPO13* gene promotor for JMJD6, HIF1β, HIF2α, H3K4me1, H3K4me3, H3K27ac and H3K27me3.

(C) ChIP-PCR validation of JMJD6 binding at 6 target gene promoters compared to IgG IP control, and an inactive intragenic region served as a negative control (NC), n=3.

(D and E) RTq-PCR quantification of JMJD6 target genes from 786-O cells transfected with sgCtrl or *JMJD6* sgRNAs (sg*JMJD6*-2/4) (D) or HA-JMJD6 sg2-resistant (JMJD6), catalytic dead HA-JMJD6 sg2-resistant (CD) followed by infection with sgCtrl or sg*JMJD6*-2 (E), n=3.

(F) ChIP-PCR of H3K4me3 binding at 6 target gene promoters in 786-O cells transduced with sgCtrl or JMJD6 sgRNAs (sg*JMJD6*-2/4), n=3.
Error bars represent SEM, two-tailed Student's t-test, **P*<0.05, ***P*<0.01, ****P*<0.001, *****P*<0.0001. n.s. means no significance.

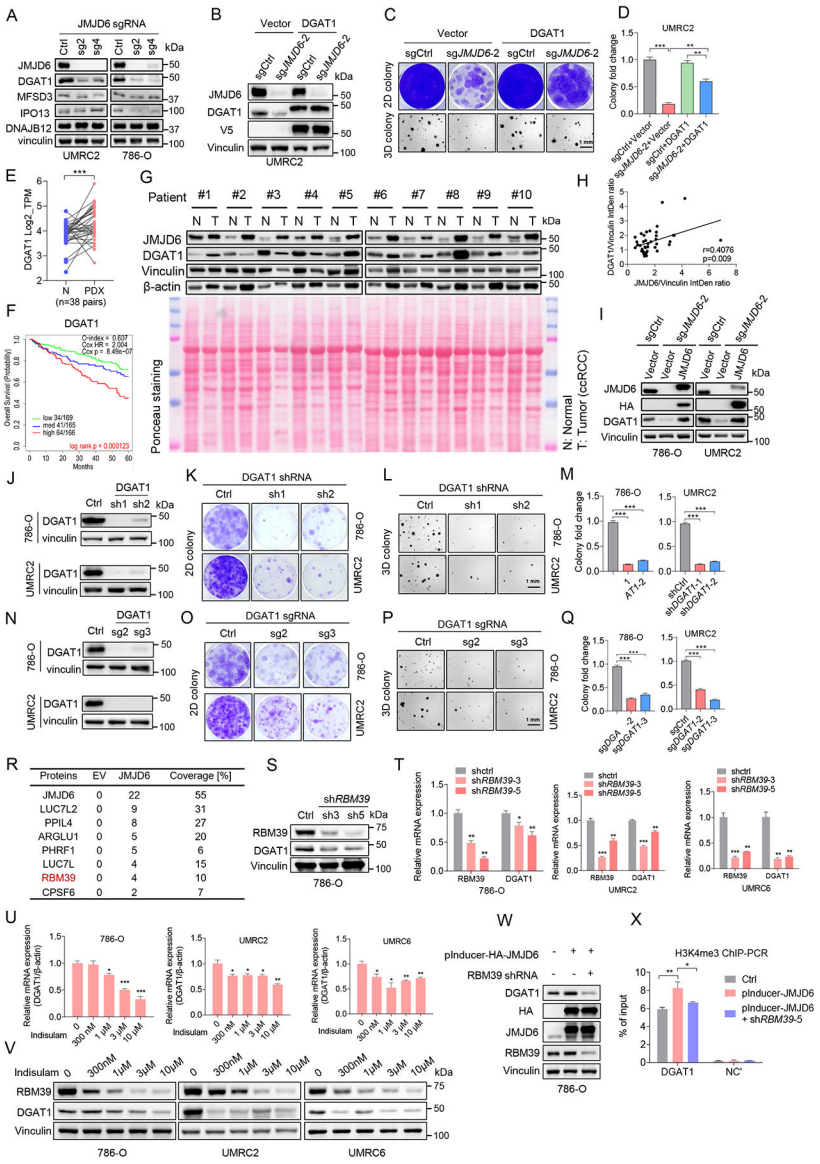

Figure 4. DGAT1 Serves as a Critical JMJD6 Effector in ccRCC

(A) Immunoblotting analysis of indicated ccRCC cell lines transduced with sgCtrl or *JMJD6* sgRNA2/4 (sg2, sg4).

(B-D) Immunoblotting (B), 2D colony formation assay and representative soft agar images (C), and corresponding quantification data (n=3) (D) in UMRC2 cells overexpressed with empty vector or DGAT1, followed by infection with lentivirus expressing sgCtrl or sg*JMJD6*-2.

(E) *DGAT1* mRNA level in paired normal (N) and patient derived xenograft (PDX) tissues, n=38.

(F) Kaplan-Meier plots of survival data for kidney cancer patients stratified by *DGAT1* mRNA expression levels.

(G) Immunoblotting for lysates from indicated ccRCC paired patient normal (N) and tumor (T) tissues, n=10.

(H) Pearson's correlation analysis of quantified protein level between JMJD6 and DGAT1 in 20 pairs ccRCC patient normal and tumor tissues.
(I) Immunoblotting of indicated cell lines overexpressed with control (Vector) or HA-JMJD6 sg2-resistant (JMJD6), followed by infection with sgCtrl or sg*JMJD6*-2.
(J-Q) Immunoblotting (J and N), 2D colony formation assay (K and O), representative soft agar images (L and P) and corresponding quantification data (n=3) (M and Q) in indicated cell lines transduced with either shCtrl or *DGAT1* shRNAs or sgRNAs.
(R) Lists of JMJD6 binding proteins identified by mass spectrometry (MS). RBM39 is a JMJD6 interactor identified by further immunoprecipitation confirmation followed by MS.
(S and T) Immunoblotting (S) and RT-qPCR quantification (T) of indicated cell lines infected with shCtrl or sh*RBM39*-3/5.
(U and V) RT-qPCR quantification (U) and immunoblotting (V) of indicated cell lines treated with indisulam at indicated concentration for 48h.
(W and X) Immunoblotting (W) and ChIP-PCR of H3K4me3 binding at *DGAT1* gene promoters in 786-O cells infected with empty vector or pInducer-JMJD6 followed by infection with shCtrl or sh*RBM39*-5. A region located near *DGAT1* that has negative-looking signal serves as a negative control (NC').
Error bars represent SEM, two-tailed Student's t-test, **P*<0.05, ***P*<0.01, ****P*<0.001.

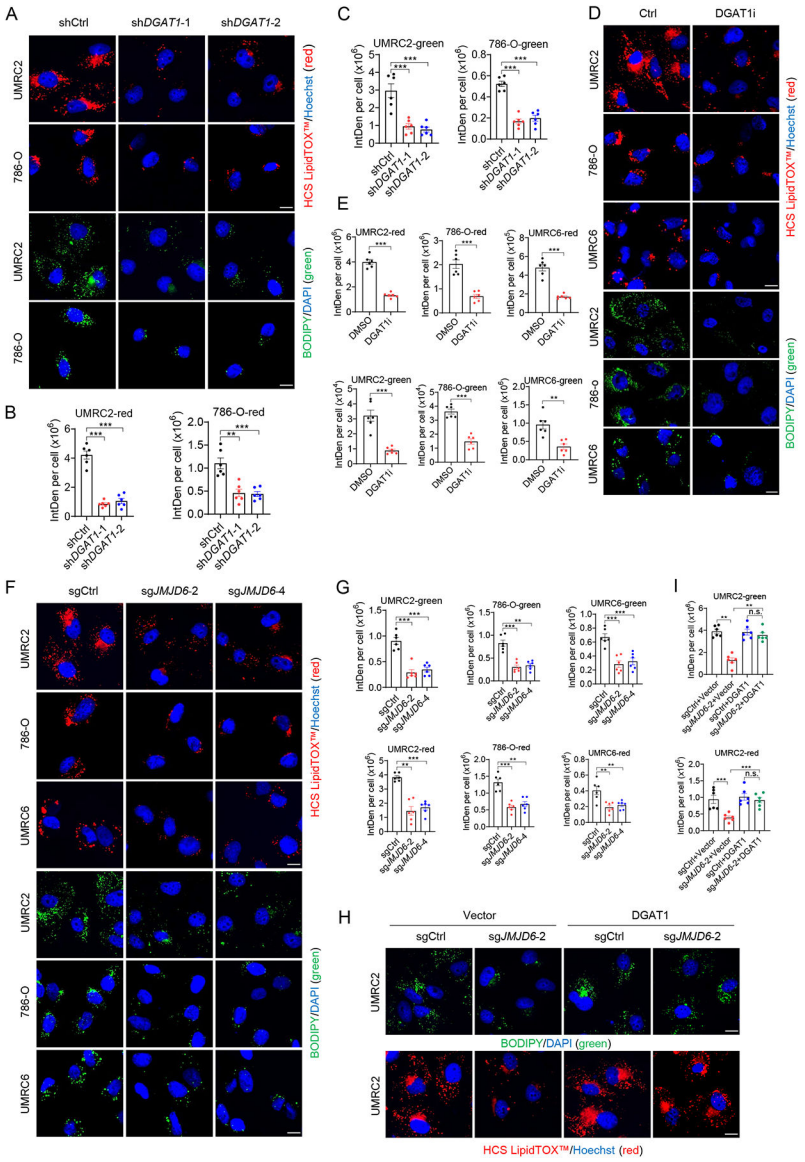

Figure 5. JMJD6 Promotes Lipid Droplet Formation via DGAT1 in ccRCC

(A-C) Representative fluorescence imaging (n=6 images in total) (A) of lipid droplets stained with HCS LipidTOX™ (red) or BODIPY 493/503 (green), and corresponding quantification data (red-B, green-C) in indicated cell lines transduced with shCtrl or DGAT1 shRNA1/2. Nuclei were stained with Hoechst 33342 or DAPI (blue).

(D and E) Representative fluorescence imaging (n=6 images in total) (D) of lipid droplets stained with HCS LipidTOX™ (red) or BODIPY 493/503 (green), and corresponding quantification data (E) in indicated cell lines treated with DMSO (Ctrl) or DGAT1 inhibitor A922500 (DGAT1i, 40 μM) for 24 h. Nuclei were stained with Hoechst 33342 or DAPI (blue).

(F and G) Representative fluorescence imaging (n=6 images in total) (F) of lipid droplets stained with HCS LipidTOX™ (red) or BODIPY 493/503 (green), and corresponding quantification data

(G) in indicated cell lines transduced with sgCtrl or JMJD6 sgRNA2/4. Nuclei were stained with Hoechst 33342 or DAPI (blue).

(H and I) Representative fluorescence imaging ((n=6 images in total)) (H) of lipid droplets stained with BODIPY 493/503 (green) or HCS LipidTOX™ (red), and corresponding quantification data (I) in UMRC2 cells overexpressed with empty vector (Vec) or DGAT1, followed by infection with sgCtrl or JMJD6 sg2. Nuclei were stained with Hoechst 33342 or DAPI (blue).

Error bars represent SEM, two-tailed Student's t-test. Scale bar, 50 μm. $^{**}P<0.01$, $^{***}P<0.001$. n.s. means no significance.

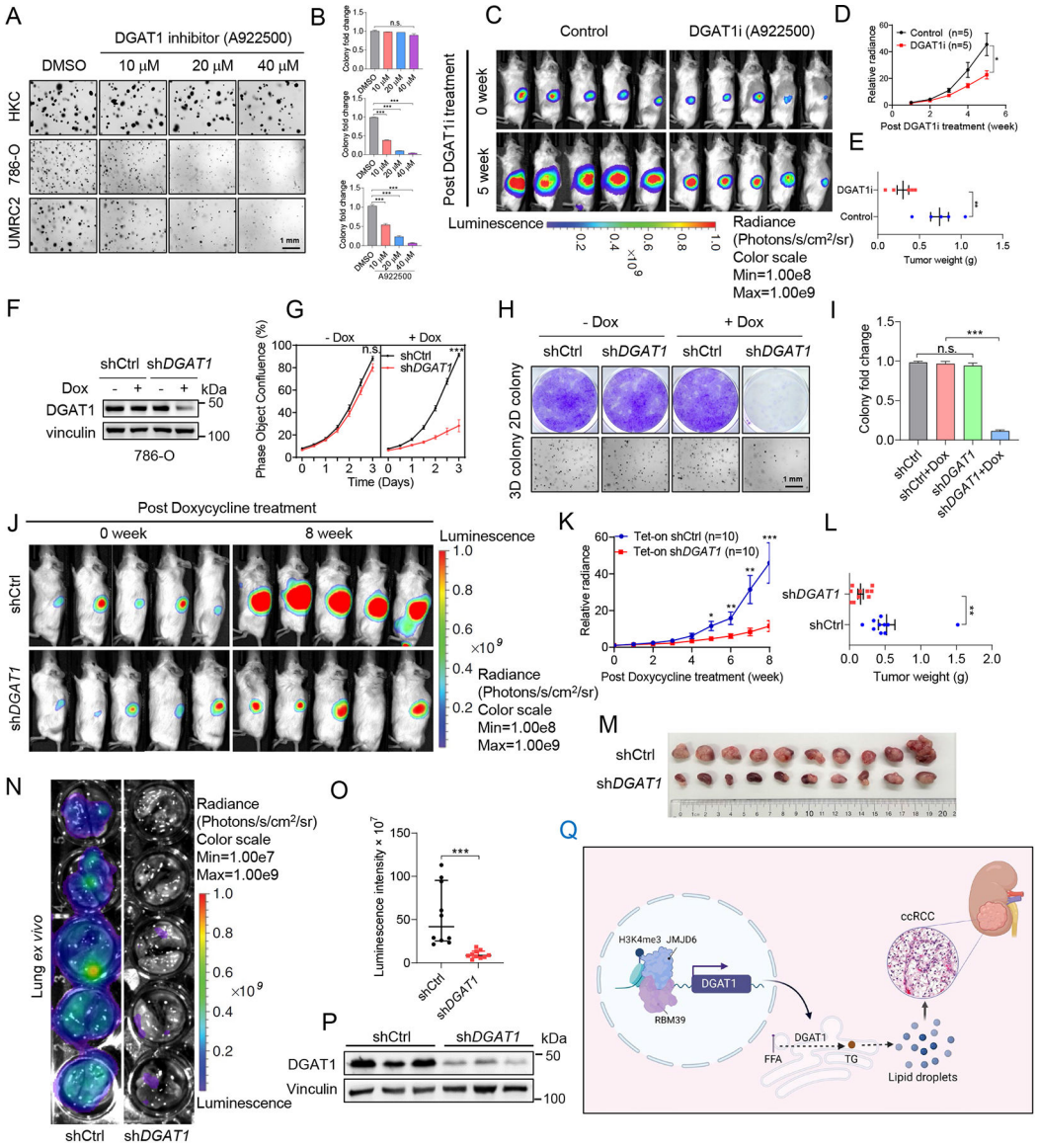

Figure 6. DGAT1 Inhibition Reduces Tumor Growth in ccRCC Models

(A and B) Representative soft agar images (A) and colony quantification (n=3) (B) in indicated cell lines treated with DMSO or DGAT1 inhibitor A922500 (10/20/40 μM) for 14days.

(C-E) Representative bioluminescence imaging (C) of before (0 week) and 5 weeks post DGAT1 inhibitor A-922500 (60mg/kg/day, oral gavage), quantification of post-DGAT1i treatment bioluminescence imaging (D), tumor weight after dissection (E) in 786-O-derived orthotopic model (NSG, n=5).

(F-I) Immunoblotting (F), incucyte cell proliferation assay (n=5) (G), 2D colony formation assay and representative soft agar images (H), and colony quantification (n=3) (I) in 786-O luciferase stable cell lines transduced with teton-control shRNA (shCtrl) or teton-*DGAT1* shRNA (sh*DGAT1*) and treated with or without doxycycline as indicated.

(J-P) Representative bioluminescence imaging of before (0 week) and 8 weeks post-doxycycline treatment (J), quantification of post-doxycycline treatment bioluminescence imaging (K), tumor weight (L), image of tumors (M) after dissection, representative lung *ex vivo* bioluminescence imaging (N) and corresponding quantification (O), immunoblotting analysis (P) from 786-O luciferase stable cells transduced with lentivirus expressing either Teton control (shCtrl) or teton-DGAT1 shRNA (sh*DGAT1*) that were injected orthotopically into the renal sub-capsule of NSG mice (n=10).

(Q) Schematics or JMJD6-DGAT1 signaling axis in ccRCC. JMJD6 interacts with RBM39 and occupies target gene promoters along with H3K4me3 and activates DGAT1 expression, which contributes to increased triglyceride (TG), lipid droplet formation and ccRCC tumorigenesis.

Error bars represent SEM, two-tailed Student's t-test, *P<0.05, **P<0.01, ***P<0.001. n.s. means no significance.

KEY RESOURCES TABLE

REAGENT or RESOURCE	SOURCE	IDENTIFIER
Antibodies		
Rabbit anti-JMJD6 for WB and IHC	Cell Signaling Technology	Cat# 60602; RRID: AB_2799591
Rabbit anti-JMJD6 for ChIP and IP	Abcam	Cat# ab64575; RRID: AB_1280968
Rabbit anti-HA-Tag	Cell Signaling Technology	Cat# 3724; RRID: AB_1549585
Rabbit anti-H3K4me3-ChIP Grade	Abcam	Cat# ab8580; RRID: AB_306649
Rabbit anti-V5-Tag	Cell Signaling Technology	Cat# 13202; RRID: AB_2687461
Rabbit anti-DGAT1	Abcam	Cat# ab181180
Rabbit anti-RNA polymerase II	Abcam	Cat# ab264350
Rabbit anti-MFSD3	NOVUS Biologicals	Cat# NBP2-83199
Rabbit anti-IPO13	NOVUS Biologicals	Cat# NBP1-31508; RRID: AB_2296220
Rabbit anti-DNAJB12	ProteinTech	Cat# 16780-1-AP; RRID: AB_2094404
Rabbit anti-PHRF1	Abcam	Cat# ab85974; RRID: AB_1925150
Rabbit anti-CPSF6	Abcam	Cat# ab175237; RRID: AB_2861386
Rabbit anti-RBM39	Sigma-Aldrich	Cat# HPA001591; RRID: AB_1079749
Rabbit anti-H4R3me2s	Thermo Fisher Scientific	Cat# 61188
Rabbit anti-Histone 4	ProteinTech	Cat# 16047-1-AP; RRID: AB_2118625
Mouse anti-SET1A	Santa cruz	Cat# sc-515590
Mouse anti-MLL (H-10)	Qin Yan lab	Cat# sc-374392; RRID: AB_10988264
Rabbit anti-MLL2	Qin Yan lab	Cat# 63735; RRID: AB_2737357
Mouse anti-MLL-C	Weibo Luo lab	Cat# 05-765
Mouse anti-ARNT1/HIF-1b	BD Biosciences	Cat# 611078; RRID: AB_398391
Rabbit anti-VHL	Cell Signaling Technology	Cat# 68547; RRID: AB_2716279
Rabbit anti-HIF-2alpha	Cell Signaling Technology	Cat# 7096; RRID: AB_10898028
Normal Rabbit IgG	Cell Signaling Technology	Cat# 2729; RRID: AB_1031062
Mouse anti-alpha-Tubulin	Cell Signaling Technology	Cat# 3873; RRID: AB_1904178
Mouse anti-β-Actin	Cell Signaling Technology	Cat# 3700; RRID: AB_2242334
Mouse anti-Vinculin	Sigma-Aldrich	Cat# V9131; RRID: AB_477629
Rat anti-HA affinity matrix	Millipore Sigma	Cat# 11815016001; RRID: AB_390914
Mouse anti-FLAG M2 Affinity Gel	Sigma-Aldrich	Cat# A2220, RRID: AB_10063035
Dynabeads™ M-280 sheep anti-rabbit IgG	Thermo Fisher Scientific	Cat# 11203D; RRID: AB_2783009
HRP-conjugated goat anti-mouse	Thermo Fisher Scientific	Cat# 31430; RRID: AB_228307
HRP-conjugated goat anti-rabbit IgG	Thermo Fisher Scientific	Cat# 31460; RRID: AB_228341
Bacterial and virus strains		
MAX Efficiency™ DH5α Competent Cells	Thermo Fisher Scientific	Cat# 18258012
One Shot™ Stbl3™ Chemically Competent *E. coli*	Thermo Fisher Scientific	Cat# C737303
One Shot™ ccdB Survival™ 2 T1R Competent Cells	Thermo Fisher Scientific	Cat# A10460

REAGENT or RESOURCE	SOURCE	IDENTIFIER
XL10-Gold Ultracompetent Cells	Agilent Technologies	Cat# 200315
lentiCRISPR v2	Addgene	Cat# 52961
Tet-pLKO-puro	Addgene	Cat# 21915
pInducer20	Addgene	Cat# 44012
Biological samples		
Human ccRCC paired tissues	Tissue procurement facility at UNC	N/A
Human ccRCC paired tissues and IHC slides	UTSW Tissue Management Shared Resource Center	N/A
Patient-derived xenografts (PDX)	human renal cell carcinoma tumorgraft platform for preclinical drug testing in UTSW	N/A
Chemicals, peptides, and recombinant proteins		
Iodonitrotetrazolium chloride	Sigma-Aldrich	Cat# I8377
MTS reagents	Abcam	Cat# ab197010
Crystal violet	Sigma-Aldrich	Cat# C-6158
Doxycycline	Sigma-Aldrich	Cat# D9891
D-Luciferin-potassium salt	Goldbio	Cat# LUCK-1G
Ponceau S	Sigma-Aldrich	Cat# P3504
BODIPY™ 493/503	Thermo Fisher Scientific	Cat# D3922
HCS LipidTOX™ Red	Thermo Fisher Scientific	Cat# H34476
DAPI	Sigma-Aldrich	Cat# D9542
Hoechst 33342	Fisher Scientific	Cat# H3570
A922500	MedChem Express	Cat# HY-10038
WL12	Axon Med Chem	Cat# 899548-78-8
ETO	MedChem Express	Cat# HY-50202A
RNase	Roche	Cat# 11119915001
Proteinase K	Sigma-Aldrich	Cat# 3115828001
polybrene	Santa Cruz Biotechnology	Cat# sc-134220
RNAiMAX transfection reagent	Thermo Fisher Scientific	Cat# 13778150
MitoSOX™ Red Mitochondrial Superoxide Indicator	Thermo Fisher Scientific	Cat# M36008
matrigel	Corning	Cat# 354234
Triacsin C	Mike Henne lab (Piccolis et al., 2019)	Cat# sc-200574A
Indisulam	Nijhawan Lab (Han et al., 2017)	N/A
Puromycin	GIBCO	Cat# A11138-03
Hygromycin	Invitrogen	Cat# 10687010
G418 Sulfate	Thermo Fisher Scientific	Cat# 10-131-027
Lipofectamine 3000 transfection reagent	Thermo Fisher Scientific	Cat# L3000015
Critical commercial assays		

REAGENT or RESOURCE	SOURCE	IDENTIFIER
RNeasy mini kit	Qiagen	Cat# 74106
iScript™ cDNA Synthesis Kit	Bio-Rad	Cat# 1708891
Quick Change XL Site-Directed Mutagenesis Kit	Agilent Technologies	Cat# 200516
SimpleChIP® Enzymatic Chromatin IP Kit	Cell Signaling Technology	Cat# 9003
NEBNext® Ultra™ II DNA Library Prep Kit	New England Biolabs	Cat# E7645S
triglyceride quantification colorimetric/ fluorometric kit	Sigma-Aldrich	Cat# MAK266
FITC Annexin V Apoptosis Detection Kit with PI	Biolegend	Cat# 640914
RNase-Free DNase Set	QIAGEN	Cat# 79256
KOD -Plus- Mutagenesis Kit	Toyobo	Cat# SMK-101
Deposited data		
JMJD6 ChIP-seq data	This paper	GSE182888
JMJD6 RNA-seq data	This paper	GSE182888
Mass spectrometry data	This paper	Suppl. table 2
Mendeley Database	This paper	https://data.mendeley.com/datasets/k46xbs8b3s/draft?a=8df74bbf-6b1b-46e5-8f32-0f512edba78f
Experimental models: Cell lines		
786-O	ATCC	CRL-1932
A498	ATCC	HTB-44
293T	ATCC	CRL-3216
UMRC2	Sigma-Aldrich	Cat# 08090511
UMRC6	Sigma-Aldrich	Cat# 08090513
HKC	W. Kimryn Rathmell Lab	N/A
Experimental models: Organisms/strains		
NOD SCID Gamma mice	Animal Resource Center (ARC) at UTSW	N/A
Oligonucleotides		
Non-targeting siRNA	Dharmacon	Cat# D0012100220
CPSF6 siRNA- 1	Thermo Fisher Scientific	s21773
CPSF6 siRNA- 2	Thermo Fisher Scientific	s21774
CPSF6 siRNA- 3	Thermo Fisher Scientific	s21775
CPSF6 siRNA- 4	Thermo Fisher Scientific	s223186
All other siRNA targeting sequence, see Table S1	This paper	N/A
JMJD6 shRNA3	Millipore Sigma	TRCN0000063339
JMJD6 shRNA4	Millipore Sigma	TRCN0000063340
RBM39 shRNA3	UNC lenti-shRNA Core Facility	TRCN0000021772
RBM39 shRNA5	UNC lenti-shRNA Core Facility	TRCN0000021769

REAGENT or RESOURCE	SOURCE	IDENTIFIER
DGAT1 sgRNA2/shRNAs	Deliang Guo lab (Cheng et al., 2020)	N/A
Primers for RT-qPCR, see Table S4	This paper	N/A
Primers for ChIP-qPCR, see Table S5	This paper	N/A
JMJD6 sgRNA-2 targeting sequence: TGAAAGACCTTACAAGCCCG	This paper	N/A
JMJD6 sgRNA-4 targeting sequence: GTATGGCACAAGACGGTAAG	This paper	N/A
DGAT1 sgRNA-3 targeting sequence: CGGCGGCGGAAGAGGAGGTG	This paper	N/A
Tet-on JMJD6 shRNA targeting sequence: CGATGGCTACTCAGTGAAGAT	This paper	N/A
Recombinant DNA		
DGAT1 cDNA clone	GeneCopoeia	Cat# EX-Z9248-LX304
MFSD3 in pLenti6.3/V5-DEST	DNASU	Cat# HsCD00866262
pLX307-mCherry-ZSWIM8	Joshua Mendell lab (Han et al., 2020)	N/A
DNAJB12 in pDONR223	DNASU	Cat# HsCD00352383
IPO13 in pDONR221	DNASU	Cat# HsCD00861619
plenti-UBCp-FLAG-HA-JMJD6	This paper	N/A
pInducer-JMJD6-sg2-resistant	This paper	N/A
pInducer-JMJD6-CD (H187A/D189A) -sg2-resistant	This paper	N/A
pInducer-JMJD6	This paper	N/A
pInducer-JMJD6-CD (H187A/D189A)	This paper	N/A
Software and algorithms		
Fiji, ImageJ	ImageJ	https://imagej.net/Downloads
GraphPad Prism 9	GraphPad	https://www.graphpad.com/scientific-software/prism/
Other		
XF24 cell culture microplate	Agilent	Cat# 102720-100
DMEM, no glucose, no glutamine, no phenol red	Thermo Fisher Scientific	Cat# A1443001
Purina rodent chow doxycycline	Research Diets	Cat# C11300-2000i
Gateway™ BP Clonase™ II Enzyme mix	Fisher Scientific	Cat# 11-789-020
Gateway™ LR Clonase™ II Enzyme mix	Fisher Scientific	Cat# 11-791-100
Tet system approved FBS	Takara Bio	Cat# 631105
high sensitivity D1000 reagents	Agilent Technologies	Cat# 5067-5585
high sensitivity D1000 screen tape	Agilent Technologies	Cat# 5067-5584
ECL	Bio-Rad	Cat# 1705061
SuperSignal™ West Femto maximum sensitivity substrate	Thermo Fisher Scientific	Cat# 34096
NEBNext Multiplex Oligos for Illumina	New England Biolabs	Cat# E7335S